

# Radiation fields in star-forming galaxies: the disk, thin disk and bulge<sup>★</sup>

Cristina C. Popescu<sup>1†</sup> and Richard J. Tuffs<sup>2‡</sup>

<sup>1</sup> *Jeremiah Horrocks Institute, University of Central Lancashire, PR1 2HE, Preston, UK*

<sup>2</sup> *Max Planck Institut für Kernphysik, Saupfercheckweg 1, D-69117 Heidelberg, Germany*

Accepted 2013 September 1. Received 2013 September 1; in original form 2013 March 25

## ABSTRACT

We provide and describe a library of diffuse stellar radiation fields in spiral galaxies derived using calculations of the transfer of stellar radiation from the main morphological components - disks, thin disks, and bulges - through the dusty interstellar medium. These radiation fields are self-consistent with the solutions for the integrated panchromatic spectral energy distributions (SEDs) previously presented using the same model. Because of this, observables calculated from the radiation fields, such as gamma-ray or radio emission, can be self-consistently combined with the solutions for the ultraviolet/optical/submillimeter SEDs, thus expanding the range of applicability of the radiation transfer model to a broader range of wavelengths and physical quantities. We also give analytic solutions for radiation fields in optically thin stellar disks, in stellar disks with one dust disk and in stellar disks with two dust disks. The analytic solutions for the direct light are exact and can be used as benchmarks. The analytic solutions with scattering are only approximate, becoming exact only in the extreme optically thick limit. We find strongly contrasting solutions for the spatial distribution of the radiation fields for disks, thin disks and bulges. For bulges we find a strong dependence of the radiation fields on Sérsic index.

**Key words:** radiative transfer – dust, extinction - galaxies: ISM – galaxies: spiral – galaxies: stellar content

## 1 INTRODUCTION

Knowledge of radiation fields (RF) in galaxies is of prime importance to many branches of astrophysics, embracing low- and high-energy processes in the interstellar and intergalactic medium, with applications to cosmology, galactic astrophysics, astro-chemistry and astro-biology. For example ultraviolet (UV) radiation fields are one of the most important heating agents for interstellar gas, proceeding either through photoionisation in the presence of ionising UV radiation, or through the photoelectric effect in the neutral ISM. Thus, the main cooling lines of the interstellar medium, in particular the [CII] line, are produced as a result of the photoelectric effect on dust grains, primary driven by non-ionising UV photons from the ambient radiation fields interacting with polycyclic aromatic hydrocarbon (PAH) molecules and dust grains, both in star-formation regions (e.g. Crawford et al. 1985, Tielens & Hollenbach 1985, Wolfire et al. 1989, Hollenbach 1991, Israel & Maloney 2011) and in the diffuse ISM (e.g. Madden et al. 1993, Bennett et al. 1994, Pierini et al. 1999, Pierini et al. 2001, Rubin et al. 2009, Lebouteiller et al. 2012). Diffuse RFs impinging on

molecular clouds in the interstellar medium also drive the excitation of molecules in the outer layers of the clouds, determining the rotational-line emission from rare tracers such as CO molecules, from which the bulk of the mass in the form of molecular hydrogen can be determined. A quantitative knowledge of the amplitude and spectrum of the RFs is also a necessary input for hydro-dynamical simulations of the turbulent structure of the interstellar medium (e.g. de Avillez & Breitschwert 2007).

In high-energy astrophysics it is particularly important to know the number density of all photons, including those of low energies where the number density is high, because such photons can be transformed into gamma-rays through the inverse Compton scattering (ICS) with relativistic electrons. Indeed, inverse Compton scattering provides one of the principal  $\gamma$ -ray production mechanisms (Jones 1968, Blumenthal & Gould 1970, Aharonian & Atoyan 1981, Narginen & Putanen 1993, Brunetti 2000, Sazonov & Sunyaev 2000). In a variety of astrophysics environments, from very compact objects like pulsars and active galactic nuclei to extended sources like supernova remnants and clusters of galaxies, low-energy photons are efficiently boosted to high energies through this mechanism (Aharonian & Ambartsumyan 1985, Zdziarski et al. 1989, Dermer & Atoyan 2002, Moderski et al. 2005, Khangulyan & Aharonian 2005, Kusunose & Takahara 2005, Stawarz et al. 2006, 2010). In galaxies the UV/optical and far-

<sup>★</sup> The data are available in electronic form at the CDS via anonymous ftp to cdsarc.u-strasbg.fr

<sup>†</sup> E-mail: cpopescu@uclan.ac.uk

<sup>‡</sup> E-mail: Richard.Tuffs@mpi-hd.mpg.de

infrared (FIR) interstellar radiation fields can be an important channel for the production of inverse Compton  $\gamma$ -rays. Thus, knowledge of the interstellar RFs is needed to measure the distribution of relativistic electrons in these objects, as well as to isolate other gamma-ray emissions, such as those produced in the decay of pions generated in the interaction of relativistic protons with interstellar gas. Similarly, because relativistic electrons also produce radio synchrotron emission, knowledge of the RF in galaxies is necessary to elucidate the strength of interstellar magnetic fields from a combination of radio and gamma-ray observations. Radiation fields also affect the propagation of gamma-rays through the intergalactic medium (e.g. Stecker et al. 1992) as well as even in the interstellar medium (Moskalenko et al. 2006) through pair production of gamma-ray photons on the background radiation fields.

In summary it is clear that the observational signatures of many of the most fundamental physical attributes of galaxies, including the mass of interstellar gas, in both atomic and molecular form, the thermodynamical properties of this gas, as well as the ambient magnetic fields and cosmic rays in the form of both protons and nuclei and electrons, depend on the radiation fields in galaxies. It would be relatively straightforward to determine radiation fields by direct observations of the sources of photons, which, in most cases, are predominantly stars, if galaxies were optically thin. However, galaxies - and in particular star-forming galaxies - contain dust, which, because it absorbs and scatters photons, partially or wholly prevents a direct measurement of the spatial and spectral distribution of the sources of the RFs. The propagation of light depends in a complex way on the relative distribution of stellar emissivity and dust opacity, with structures ranging in scale from parsecs to kiloparsecs. Fortunately, although dust is the cause of this problem, it is also part of the solution, because the absorbed light is re-radiated in the mid-infrared (MIR)/FIR/submillimeter (submm). In particular grains which are sufficiently large to be in equilibrium with the radiation fields directly probe the strength of these radiation fields, acting as a strong constraint on the radiation transfer problem. In addition, the radiation emitted by grains small enough to be impulsively heated by individual photons strongly depends on the colour of these photons, placing particular constraints on the UV component of the interstellar radiation fields, providing one has independent knowledge of the size distributions of the constituent populations of grains.

Thus, the key to determining radiation fields in galaxies is to invert the observed broad-band spectral energy distribution incorporating both measurements of direct light in the ultraviolet (UV)/optical, as well as the dust re-radiated light in the Far-infrared (FIR)/submillimeter (submm), self-consistently taking into account constraints on the spatial distribution of both stars and dust as well as on the optical properties of the grains. This is the only way in which the exact contribution of optical and UV photons in heating dust grains can be traced, allowing for a proper determination of the contribution of old and young stellar populations in heating the dust (Popescu & Tuffs 2010), and therefore allowing for a consistent estimation of the star-formation rates in galaxies, and, ultimately for a robust determination of their star-formation history. Self-consistent modelling of the panchromatic spectral energy distributions (SEDs) of galaxies (e.g. Rowan-Robinson & Crawford 1989, Rowan-Robinson 1992, Silva et al. 1998, Popescu et al. 2000, Efstathiou, Rowan-Robinson & Siebenmorgen 2000, Misiriotis et al. 2001, Efstathiou & Rowan-Robinson 2003, Popescu et al. 2004, Siebenmorgen & Krügel 2007, Rowan-Robinson & Efstathiou 2009, Bianchi 2008, Baes et al. 2010, Baes et al. 2011, Popescu et al. 2011, MacLachlan et al. 2011, Schechtman-Rook

et al. 2012, de Looze et al. 2012a,b) have been primarily motivated by the need to extract intrinsic parameters of the stars and dust, most notably the aforementioned SFRs, SF histories and dust masses (see also review of Rowan-Robinson 2012).

In previous papers (Popescu et al. 2000, Tuffs et al. 2004, Popescu et al. 2011) we provided self-consistent solutions for modelling the integrated panchromatic SEDs of star-forming disk galaxies. Here we give and describe the solutions for the radiation fields, implicit to the SEDs presented in our previous work. The solutions are given in the form of a library of stellar radiation fields for the main morphological components of our model of spiral galaxies: disks, thin disks and bulges. These radiation fields are identical to those used when calculating the library of panchromatic SEDs presented in Popescu et al. (2011). Because of this observables calculated from the radiation fields, such as gamma-ray or radio emission, can be self-consistently combined with the solutions for the UV/optical/submm SEDs found using Popescu et al. (2011), thus expanding the range of applicability of the radiation transfer model to a broader range of wavelengths and physical quantities. Accordingly, the library of radiation fields is calculated for different values of central face-on dust opacity, as defined in Popescu et al. (2011). The separate tabulation of the radiation fields for disks, thin disks and bulges is possible because all the stellar components are attenuated by the same distribution of dust, and therefore the diffuse radiation fields seen by each grain can be considered to be a sum of the radiation fields produced by each stellar component. Thus, the radiation fields can be combined according to other model parameters from Popescu et al. (2011): the bulge-to-disk ratio ( $B/D$ ), the  $SFR$  determining the luminosity of the young stellar population (thin disk), and the parameter expressing the normalised luminosity of the old stellar population in the disk,  $old$ , to derive combined radiation fields of spiral galaxies. This concept, which relies on stellar light being an additive quantity, was originally introduced in Tuffs et al. (2004) to describe the attenuation of stellar light. Here we only show radiation fields in direct stellar light (UV/optical/NIR), as these are the ones that can be separately calculated and have additive properties. Radiation fields in dust re-emission will be the object of a future paper, as these cannot be separated according to the different stellar components heating the dust, nor have they additive properties. This is because there is no linear transformation between dust emission and absorption. For all these reasons, the radiation fields in dust re-emission can only be presented as combined radiation fields, characteristic of a galaxy as a whole.

This paper is organised as follows. The general characteristics of the calculations are presented in Sect. 2. In Sect. 3 we present the library of radiation fields and show how the energy densities should be scaled according to the size and luminosity of a given galaxy. In Sect. 4 we derive analytic solutions for the mid-plane radiation fields of stellar disks with and without dust, which we use to check the accuracy of our radiative transfer calculations for the particular cases covered by the analytic solutions. In Sect. 5 we describe the spatial variation of the radiation fields for each morphological component, referring to the analytic solutions to analyse the physical factors involved in shaping these variations. In Sect. 6 we correspondingly analyse the variation of the radiation fields with face-on dust opacity. For the specific case of bulge radiation fields we also describe in Sect. 7 the change in energy densities when changing the Sérsic index of the volume stellar emissivity and apply these results to predict the corresponding variation in heating of dust by bulge stellar populations in Sect. 8. We summarise the paper in Sect. 9.

## 2 SIMULATIONS

The simulated radiation fields are those used to generate the large library of dust- and PAH-emission SEDs presented in Popescu et al. (2011). This library is self-consistently calculated with the corresponding library of dust attenuations first presented in Tuffs et al. (2004) and then in updated form in Popescu et al. (2011). The details of the calculations leading to the production of the radiation fields are described at length in Popescu et al. (2011). Here we only briefly mention their main characteristics. All calculations were made using a modified version of the ray-tracing radiative transfer code of (Kylafis & Bahcall (1987)), which treats scattering utilising the method of scattered intensities (Kylafis & Xilouris 2005), and the dust model from Weingartner & Draine (2001) and Draine & Li (2007), incorporating a mixture of silicates, graphites and PAH molecules.

The radiation fields are calculated separately for the old stellar disk (“the disk”), the bulge and the young stellar disk (“the thin disk”) of a galaxy, all seen through a common distribution of dust. The geometrical model of Popescu et al. (2011) consists of both of a large-scale distribution of diffuse dust and stars, as well as of a clumpy component physically associated with the star-forming complexes. For the purpose of this study only the large-scale distribution of diffuse dust is considered, as it is this that affects the large-scale distribution of UV/optical light determining the values of the diffuse radiation fields.

The intrinsic volume stellar distributions are described by exponential functions in both radial and vertical direction for the two stellar disks and by deprojected de Vaucouleurs or Sérsic functions for the bulges. The diffuse dust is distributed in two disks associated with the old and young stellar populations, which we refer to as the thick and thin dust disk, respectively, on account of the different thickness of these structures. These dust distributions are described by double (radial and vertical) exponential functions. The thick dust disk is less opaque than the thin dust disk, with the relative face-on central dust opacity being fixed to a value of 0.387.

The length parameters of the model describing the volume emissivity for stars and dust - scale-lengths, scale-heights and effective radii - are listed in Table 1 in Tuffs et al. (2004). The relevant information for this work is that the old stellar disk component has a scale-length that decreases with increasing optical/NIR wavelength, as given in Table 2 in Tuffs et al. (2004), while the scale-height remains constant over this wavelength range. Similarly, the effective radius of the bulge does not vary with optical/NIR wavelength. The bulge is an oblate ellipsoid with an axial ratio (thickness) of 0.6. The young stellar disk has a much smaller scale-height than the older stellar disk (by a factor of 4.6), while its scale-length is constant over wavelength and is equal to that of the old stellar disk in the B band.

The scale-length of the thick dust disk associated with the old stellar population is larger (by a factor of 1.4) than that of the corresponding stellar disk, while its scale-height is smaller (by a factor of 1.5) than the scale-height of the old stellar disk. In contrast, the young stellar disk spatially coincides with the associated thin dust disk (same scale-heights and -lengths). As we will see in the next sections, the different vertical structure of the two dust disks strongly influences the solution for the radiation fields. The stellar and dust emissivities of the disks are truncated at a radius of 4.78 of the exponential stellar scale-length in B-band while bulges are truncated at ten effective radii. The geometrical parameters of the model have either been empirically constrained to follow the median trends found by Xilouris et al. (1999) for a sample of well

resolved edge-on spiral galaxies, including NGC891, or have been fixed from physical considerations. The physical interpretation of this model is described at length in Tuffs et al. (2004) and Popescu et al. (2011). A schematic representation of the geometrical model can be found in Fig. 1 in Popescu et al. (2011).

The radiation fields are sampled on an irregular grid with sampling intervals in radial direction ranging from 50 pc in the centre to up to 2 kpc in the outer disk and with sampling intervals in vertical direction ranging from 50 pc in the plane to up to 500 pc in the outer halo. This scheme was necessary to properly sample the radiation fields in the more optically thick central regions, where the dust associated with the thin stellar disk in conjunction with the strong positional dependence of the emissivity of the young stellar population (in  $z$ ) and the inner emissivity cusp of the bulge (in both  $R$  and  $z$ ) can lead to quite small scale structures even in the diffuse radiation fields.

## 3 THE LIBRARY OF RADIATION FIELDS

We have created a library of diffuse radiation fields, calculated on a cylindrical grid ( $R, z$ ). The radiation fields are given for different values of central face-on dust opacity in the B-band  $\tau_B^f$ , which is the only parameter of the model shaping the spatial variation of the RFs. Since the energy densities of the radiation fields are additive quantities, they scale with the spatially integrated luminosity density at a given wavelength. Therefore we only calculate RFs for a fixed reference luminosity density. The radiation fields are separately calculated for the disk, thin disk and bulge. For the bulge we considered calculations for different values of the Sérsic index of the bulge.

In total we performed calculations for seven values of the central face-on dust opacity,  $\tau_B^f = 0.1, 0.3, 0.5, 1.0, 2.0, 4.0, 8.0$ . Solutions for other values of  $\tau_B^f$ , such as for the case  $\tau_B^f = 3.5$  used to illustrate the solutions in this paper, can be found by interpolation. We considered four values for the Sérsic index of the bulge,  $n = 1, 2, 4, 8$ . At each wavelength we therefore have 7 (for  $\tau_B^f$ )  $\times$  2 (for disk and thin disk) + 7 (for  $\tau_B^f$ )  $\times$  4 (for Sérsic indices of bulge) = 42 combinations at each sampled UV/optical/NIR wavelength. We considered calculations at 15 different wavelengths, ranging from 912 Å to 5  $\mu\text{m}$ , as listed in Table E.2 of Popescu et al. (2011). Thus, the library contains a total of 42  $\times$  15 = 630 files with two-dimensional spatial grids of energy densities of the RFs.

As mentioned before, the radiation fields have been calculated for a reference spatially integrated luminosity density at each wavelength and for each stellar component. The reference luminosity is defined according to two main parameters of the model of Popescu et al. (2011), the star-formation rate  $SFR$  and  $old$ . The  $SFR$  is a parameter defining the luminosity of the young stellar populations and  $old$  is a parameter defining the luminosity of the old stellar population. Because the reference luminosity densities have been defined to correspond to the unit values of the two model parameters,  $SFR = 1 M_\odot/\text{yr}$  and  $old = 1$ , they are referred to as *unit intrinsic spectral luminosity densities* of the young and old stellar populations,  $L_{\nu,unit}^{young}$  and  $L_{\nu,unit}^{old}$ , as defined in Sect. 2.3 and Table E.2 of Popescu et al. (2011). Correspondingly, because the energy densities of the radiation fields are calculated for the unit  $L_{\nu,unit}^{young}$  and  $L_{\nu,unit}^{old}$ , they are referred to as the *unit radiation fields*, as defined in Sect. 2.5.2 of Popescu et al. (2011):  $u_{\lambda,unit}^{disk}$ ,  $u_{\lambda,unit}^{old}$  and  $u_{\lambda,unit}^{bulge}$ . The unit radiation fields are calculated for a reference disk size, as defined in Popescu et al. (2011). The reference size is  $h_{s,ref} = 5670$  pc, defined

as the intrinsic radial scale-length of the volume stellar emissivity of the disk in the B-band.

Thus, the  $u_{\lambda,unit}^{disk}$  are calculated for a thin stellar disk having  $L_{\nu,unit}^{young}$  within the truncation radius of  $4.78 \times h_{s,ref}$  (27.1 kpc); the  $u_{\lambda,unit}^{disk}$  are calculated for a stellar disk having  $L_{\nu,unit}^{old}$  within the truncation radius of  $4.78 \times h_{s,ref}$  and the  $u_{\lambda,unit}^{bulge}$  are calculated for a bulge having  $L_{\nu,unit}^{old}$  within a truncation radius of 10 effective radii. The library of radiation fields presented in this paper and made available at CDS is therefore given in the form of unit radiation fields.

For morphological components of galaxies with different luminosities  $L_{\lambda}^{disk}, L_{\lambda}^{tdisk}, L_{\lambda}^{bulge}$  and disk sizes  $h_s$ , the radiation fields at a position  $(R, z)$  can be scaled according to the formula

$$u_{\lambda}^{disk}(R, z) = u_{\lambda,unit}^{disk}(R_{ref}, z_{ref}) * \frac{L_{\lambda}^{disk}}{L_{\lambda,unit}^{old}} * \frac{h_{s,ref}^2}{h_s^2} \quad (1)$$

$$u_{\lambda}^{tdisk}(R, z) = u_{\lambda,unit}^{tdisk}(R_{ref}, z_{ref}) * \frac{L_{\lambda}^{tdisk}}{L_{\lambda,unit}^{young}} * \frac{h_{s,ref}^2}{h_s^2} \quad (2)$$

$$u_{\lambda}^{bulge}(R, z) = u_{\lambda,unit}^{bulge}(R_{ref}, z_{ref}) * \frac{L_{\lambda}^{bulge}}{L_{\lambda,unit}^{old}} * \frac{h_{s,ref}^2}{h_s^2} \quad (3)$$

where

$$R_{ref} = R * \frac{h_{s,ref}}{h_s} \quad (4)$$

$$z_{ref} = z * \frac{h_{s,ref}}{h_s} \quad (5)$$

When combined with the solutions for the UV/optical/submm SEDs found using the library of Popescu et al. (2011), the amplitude of the radiation fields can be found by scaling the unit radiation fields according to the model parameters  $SFR, old$ , bulge-to-disk ratio  $B/D$  and the clumpiness factor  $F$ , using the prescription from Sect. 2.5.2 in Popescu et al. (2011). This allows observables calculated from the radiation fields, such as gamma-rays or radio emission, to be self-consistently combined with the solutions for the integrated SEDs, thus expanding the range of applicability of the radiation transfer model to a broader range of energies and physical quantities.

As noted in Popescu et al. (2011), in any dusty galaxy  $h_s$  will not actually be a directly observable quantity, even if the distance to the galaxy is known. As described and quantified in Möllenhoff et al. (2006) and in Pastrav et al. (2013a), the apparent size of a galaxian disk obtained from photometric fits to optical images will differ from the true size due to the stronger attenuation of light at the centre of galaxies compared to the outer regions. Furthermore, when bulge-disk decomposition is performed on dusty galaxies, there will be additional effects due to dust on the decomposition itself (Pastrav et al. 2013b), resulting in additional differences between the intrinsic and the measured sizes of the disk. Thus, when scaling radiation fields, the measured scale-length (or effective radius) of the disk should be corrected for the effects of dust. Corrections for these effects can be found in Pastrav et al. (2013a) and Pastrav et al. (2013b). Since the corrections from Pastrav et al. were derived using the same radiative transfer model as used for the calculation of the radiation fields, incorporation of these corrections in the scaling of the RFs allows for a self-consistent analysis of the integrated SEDs, structural parameters and radiation fields.

All the calculated radiation fields are made available in electronic format. Their main characteristics concerning the spatial variation, as well as the variation with dust opacity, are described in Sects. 5 and 6.

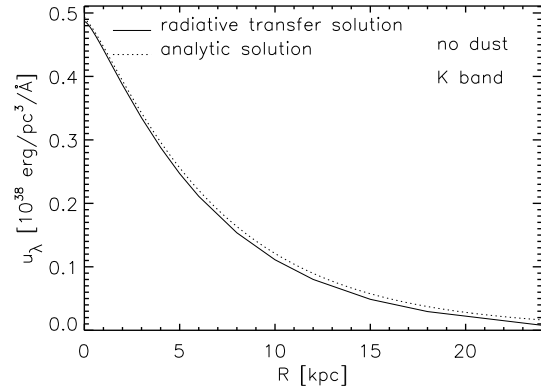


**Figure 1.** Comparison between a radial profile of radiation fields from the thin disk with no dust calculated with our radiative transfer code and the one given by the analytic formula from Eq. B10. In both cases the calculation is for the K band and  $SFR = 1 M_{\odot}/yr$ .

## 4 ANALYTIC SOLUTIONS

To check the accuracy of our radiative transfer calculations, but also to understand the trends in the variation of the radiation fields with spatial position and dust opacity, we derived analytic solutions for the energy density of the radiation fields for limiting cases. Some of the formulas (those for which we give exact solutions) can also be used as benchmark cases for testing the accuracy of different radiative transfer codes for diffuse stellar emissivities and dust distributions. We only make use of the analytic solutions for comparison with the radiative transfer solutions in the mid-plane of the disk, even though in the case of a dustless disk we have derived analytic solutions at any position.

### 4.1 An azimuthally symmetric stellar disk in the optically thin limit

In Appendix A we derive an analytic solution for the radiation fields in the mid-plane of an infinitely thin disk with no dust. This special case is instructive, as it allows the energy density in the plane of the disk to be given by the sum of two terms (Eq. A11). The first term (Eq. A14) represents the contribution of all emitting sources within a galactocentric radius  $R$ , while the second term (Eq. A15) gives the contribution of all emitting sources beyond the radius  $R$ .

For an actual comparison of the solution of the radiative transfer calculation with an analytic solution we need to also take into account the thickness of the disk in the analytic solution, as this makes a big change. We derive in Appendix B a more general formula to take this effect into account (Eq. B10.)

We show in Fig. 1 a comparison between the radial profiles predicted by the radiative transfer calculation and by the analytic formula incorporating the thin stellar disk. One can indeed see that the radiative transfer solution almost exactly follows the prediction of the analytic formula (both in amplitude and shape).

### 4.2 An azimuthally symmetric stellar disk with a dust disk

In appendix C we derive analytic solutions for the radiation fields in the mid-plane of a stellar disk with one dust disk. The solutions are derived for the case that the scale-height of the dust is equal to

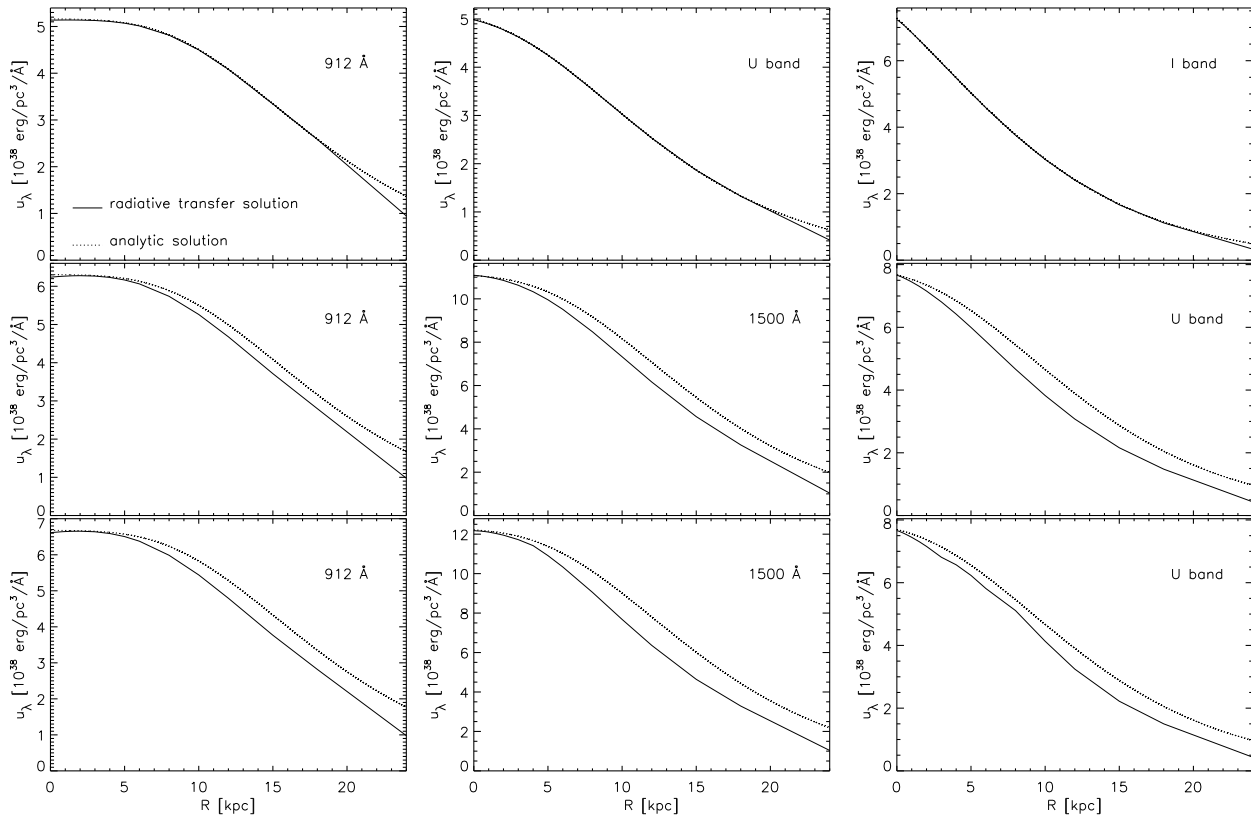


**Figure 2.** Comparison between the solutions of the analytic formula for the mid-plane radiation fields of a stellar disk with one dust disk (dotted line) and those produced from radiative transfer calculations (solid line). Top: direct light only; middle: direct plus first order scattering; bottom: total (direct plus all scattered) light. The calculations are for  $\tau_B^f = 3.5$  and  $SFR = 1 M_\odot/\text{yr}$ . The different panels show radial profiles at different wavebands.

that of the stellar disk. The calculation also assumes that the scale-height of the stellar disk is much smaller than its scale-length. In total we derive 3 formulae: one for direct light only, one for direct light plus first order scattered light and one for the total direct plus scattered light.

The formula for direct light is given by Eq. C16. This is an exact analytic formula for cases where the disk is optically thick along lines of sight in the plane of the disk. To check the validity of this formula we ran radiative transfer calculations for the geometry of the young stellar disk of our model, taking (for the purpose of this comparison) all dust to reside in the thin dust disk. Consequently, we took the scale-length of the stellar disk to be equal to that of the dust disk, even though this assumption is not required by the analytic solution. In the upper panels of Fig. 2 we show examples of calculations done for direct light only, for  $\tau_B^f = 3.5$ , for three different UV/optical wavelengths, together with the corresponding analytic solutions. One can see that the radiative transfer and the analytic solutions agree very well across the wavelength range covered by our calculations. The agreement is both in the radial dependence and in the absolute level of predicted emission. The discrepancy at larger radii is due to the inherent differences in treating the truncation of stellar and dust emissivity in vertical and radial directions in the analytic and in the radiative transfer code. The fact that the analytic formula works so well (for  $\tau_B^f = 3.5$ ) over a large range of wavelengths, from the UV to the NIR is due to the fact that the aspect ratio of our thin disk is very small, resulting in a high central edge-on dust opacity even in the NIR bands. It is only in the K band, in the centre of the profile, that a small difference

starts to occur, which is due to the fact that the solution starts to become more optically thin in radial directions. Even at  $\tau_B^f = 0.3$  the formula gives perfect agreement with the results of the 2D code between the wavelength range 912 – 4430Å. We conclude that the analytic formula for direct light can be used as a benchmark for testing radiative transfer codes for cases where the line of sight in the plane of the disk is optically thick.

The formula for direct plus first order scattered light is given by Eq. C29. This formula is an approximate one, since the term for scattering is only exact in the extreme optically thick limit. Therefore it cannot be used as a benchmark case for translucent galaxies. Nonetheless, it can be used to qualitatively explain the variation of radiation fields with spatial position and dust opacity. A comparison between the results of our RT calculations for a one dust disk case for only one order scattering and those of the analytic formula are presented in the middle row of Fig. 2. Since our radiative transfer calculations for first order scattering are exact, any departure between the predictions of the analytic formula and the RT profiles indicate the range of applicability of the formula. For very short wavelengths the formula predicts very well the shape of the inner profiles (and  $f_{esc}^1$ , as defined in the appendix, is within a few percent) where the galaxy is very optically thick, and only starts to deviate at larger radii. At longer UV wavelengths this deviation already happens for the central regions of the profiles. Nonetheless, the general trends are still well explained by the analytic formula at all wavelengths.

The formula for direct plus total scattered light is given by Eq. C30. As in the case of Eq. C29, this is also an approximation,

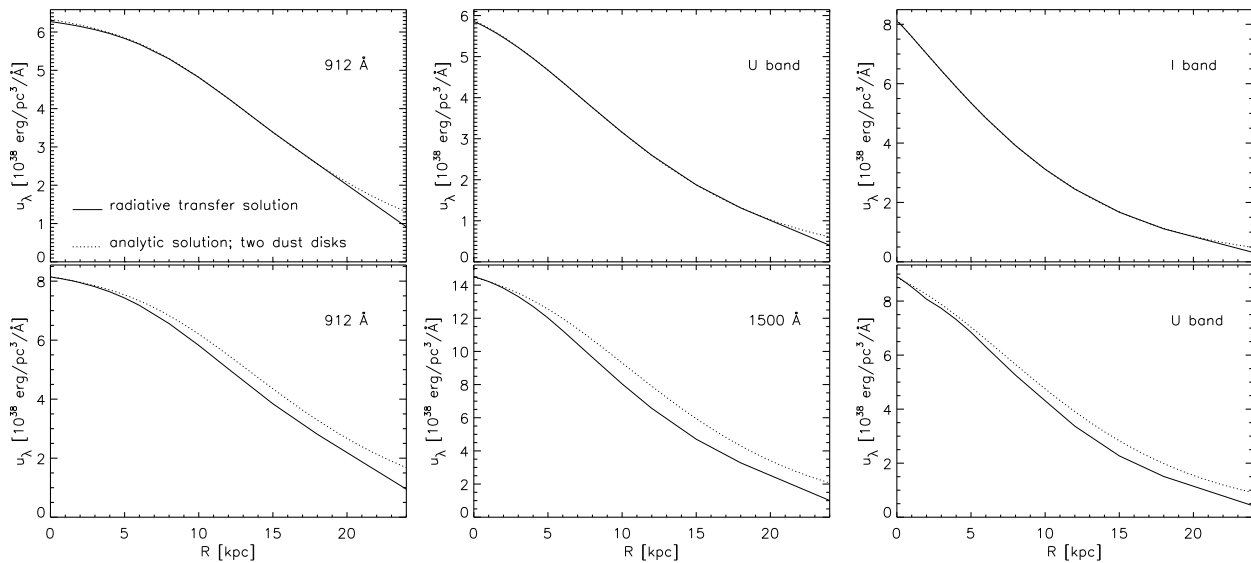


**Figure 3.** Comparison between the solutions of the exact analytic formula for the mid-plane radiation fields of a stellar disk with two dust disks (dotted line) and those produced from radiative transfer calculations (solid line). Top: direct light only; bottom: total (direct plus scattered) light. The calculations are for  $\tau_B^f = 3.5$  and  $SFR = 1M_\odot/\text{yr}$ . The different panels show radial profiles at different wavebands.

and cannot be used as a benchmark. The comparison between the radial profiles obtained from the 2D RT code and from the analytic formula (lower row of Fig 2) show the same qualitative behaviour as for the case where only first order scattering is included.

### 4.3 An azimuthally symmetric stellar disk with two dust disks

Following the same approach as for the azimuthally symmetric stellar disk with one dust disk, in appendix D we derive the corresponding analytic formulae for the case of an azimuthally symmetric stellar disk with two dust disks. This is actually the case included in our library of radiation fields, and in particular it can be used to describe our thin disk.

The exact formula for direct light is given by Eq. D20. A comparison between our 2D radiative transfer calculations and the results of this formula is given in the top row of Fig. 3, showing the same excellent agreement as found for the single dust disk case. The formula for the total radiation (direct plus scattered components) is given in Eq. D22 and the corresponding comparison with the numerical solution is given in the bottom row of Fig. 3. Although this comparison reveals a comparably good agreement in the shape of the profile as found for the case of the single dust disk, the  $f_{esc}$  in Eq. D22 takes higher values, due to a higher fraction of the dust being in an optically thin configuration.

## 5 SPATIAL VARIATION OF RADIATION FIELDS

Here we describe the spatial variation of the radiation fields of each individual stellar component of our model. Since, as mentioned before, the solutions for each component are additive, solutions for composite structures can be found by weighted addition, according to the intrinsic stellar luminosity of each component. All examples are for the case  $\tau_B^f = 3.5$ . This value of dust opacity corresponds to the solution we found for NGC 891 (Popescu et al. 2011) and for statistical samples of galaxies (Driver et al. 2007, Grootes et al. 2013).

### 5.1 The thin disk

#### 5.1.1 The radial profiles

The radial variation of the RF of the thin disk changes drastically between an optically thick and optically thin case. To illustrate this, we show in Fig. 4 examples of RFs calculated at different wavelengths. We first describe the behavior of the RF in the plane of the disk ( $z = 0$ ).

i) *The optically thin case;  $z = 0$ .* This arises at longer wavelengths, in the J and K bands, where the profile shows a monotonic decrease with increasing radial distance. For comparison, the solution with no dust at all is overplotted with a red line in the panel corresponding to the K-band. One can see that the radial profile calculated for the longer optical wavelengths and for  $\tau_B^f = 3.5$  tends towards the completely optically thin solution, which shows an even steeper decrease with increasing radial distance. This is because for a thin disk geometry the component of energy density arising from sources within galactocentric radius  $R$  tends (at high radii) towards an inverse-square law for a point source situated at  $R = 0$  and with luminosity equal to the total enclosed luminosity within  $R$ . This characteristic is explicitly seen in the formula for the exact analytic solution of an infinitely thin disk given in Eq. A11, A14, and A15. Specifically, there is an  $1/R^2$  term in front of the integral in Eq. A14 denoting the contribution to the radiation fields from emitters interior to  $R$ . This term dominates at higher radii. The second term in Eq. A11 (as given in Eq. A15) gives the contribution from sources beyond  $R$ , and dominates at low radii. This term gives a more slowly varying component for the RFs than the first term from the interior sources (Eq. A14), causing the fall-off in energy density to be shallower than an inverse square law in the inner disk. Beyond the radius enclosing half of the total luminosity, there will be a transition between the predominance of these two terms, marking the crossover to the inverse square law behaviour. This can also be seen in the comparison between the analytic and radiative transfer solutions shown in Fig. 1.

ii) *The optically thick case;  $z = 0$ .* This arises at shorter UV wavelengths, where one can see a flat profile in the inner region,

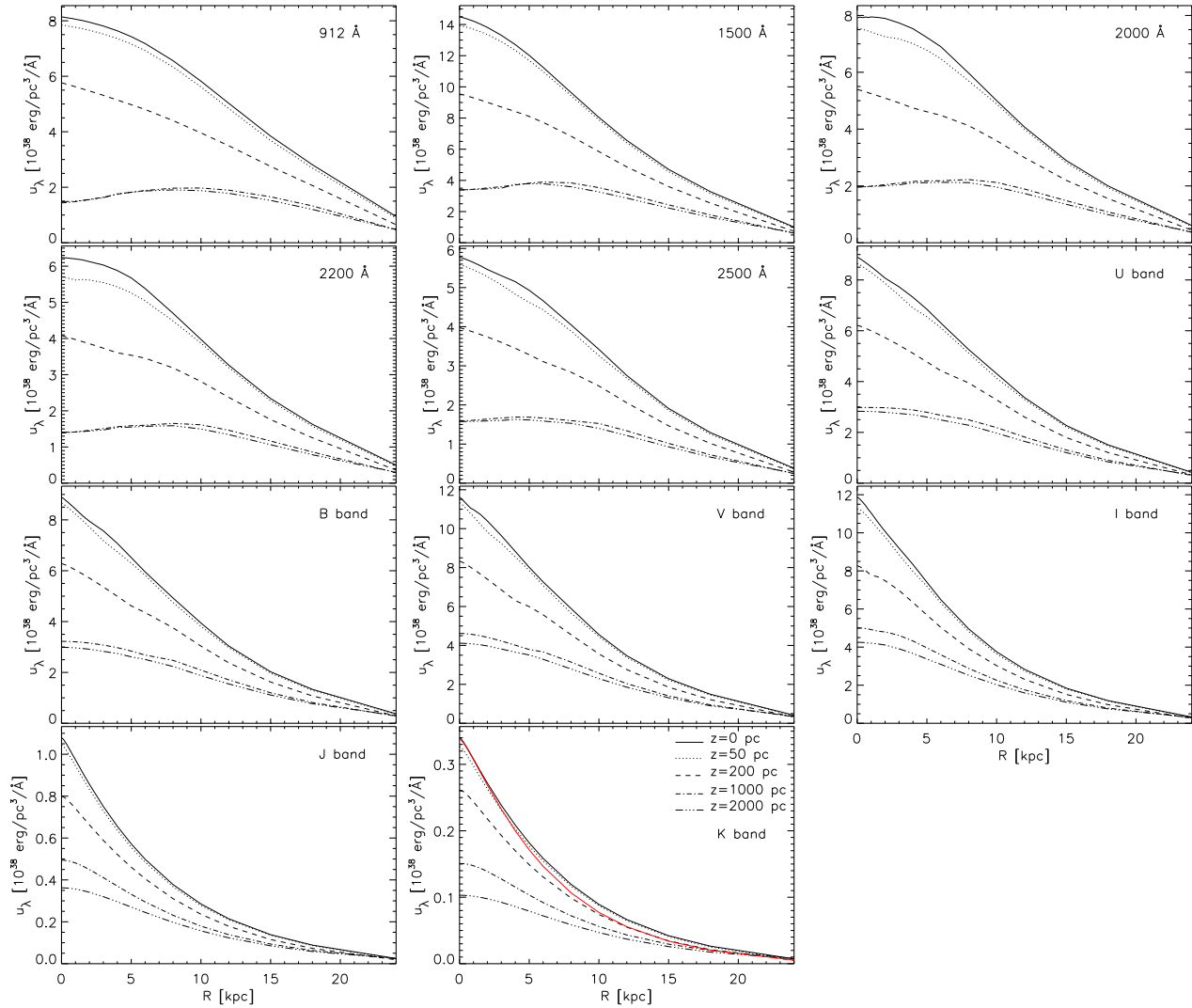


**Figure 4.** Radial profiles of unit radiation fields from the **thin disk**, for  $\tau_B^f = 3.5$ . The solid line represents the profiles in the plane ( $z = 0$  pc) while the other lines (see legend) represent profiles at different vertical distance from the plane ( $z = 50, 200, 1000$  and  $2000$  pc). The different panels show profiles at different wavebands, from the UV to the NIR. The profile overplotted in red in the bottom right panel (the K-band case) represents the dustless radiative transfer solution scaled to the  $\tau_B^f = 3.5$  solution.

followed by a monotonic decrease with increasing radial distance. The inner flat profile is a direct consequence of the optically thick character of the solution. Thus, in an optically thick case the radiation seen at each point is proportional to the stellar emissivity within the horizon sphere<sup>1</sup> define the term “horizon surface” to denote the locus of positions for which the line integral of opacity from a point within an optically thick body is unity. In the extreme optically thick case the horizon surface is a sphere, which we call “horizon sphere”. divided by the dust opacity:

$$u(R) = \frac{\eta(R)}{\kappa(R) (1 - A) c} \quad (6)$$

where  $\eta$  is the local stellar emissivity,  $\kappa$  is the local extinction coefficient (defined as the probability of extinction of a photon per unit length),  $A$  is the albedo of the dust grains and  $c$  is the speed of light. The horizon sphere is then the sphere with radius equal to  $1/\kappa$  (i.e. the typical local mean free path of photons). Eq. 6 is a

generalised version of the specific solutions for the single and two dust disks given in Eqs. C26 and D23. Eq. 6 is always valid, irrespective of geometry, for very optically thick cases. In the specific case considered here, Eq. 6 refers only to the local mid-plane volume emissivity and opacity. Thus, it will give the correct solution in all cases where the horizon is so close that any spatial variations in emissivity and opacity within the horizon can be ignored. The subtlety is that, when the horizon viewed from the mid-plane gets larger (e.g. when moving in radius towards the outer disk) Eq. 6 still gives the correct solution as long as the variation (primarily in  $z$ ) of stellar emissivity and opacity is the same. This is the case when the horizon sphere is contained within the thin disk, since both the stellar emissivity and the dust opacity have the same scale-height, and thus, the same spatial variation within the horizon sphere. Then the mid-plane RF will remain constant.

As the radial distance increases, the horizon surface starts to become a prolate ellipsoid, because light can propagate to larger distances vertically than in the radial direction before reaching the horizon (the scale-height of the dust is much shorter than its scale-

<sup>1</sup> w

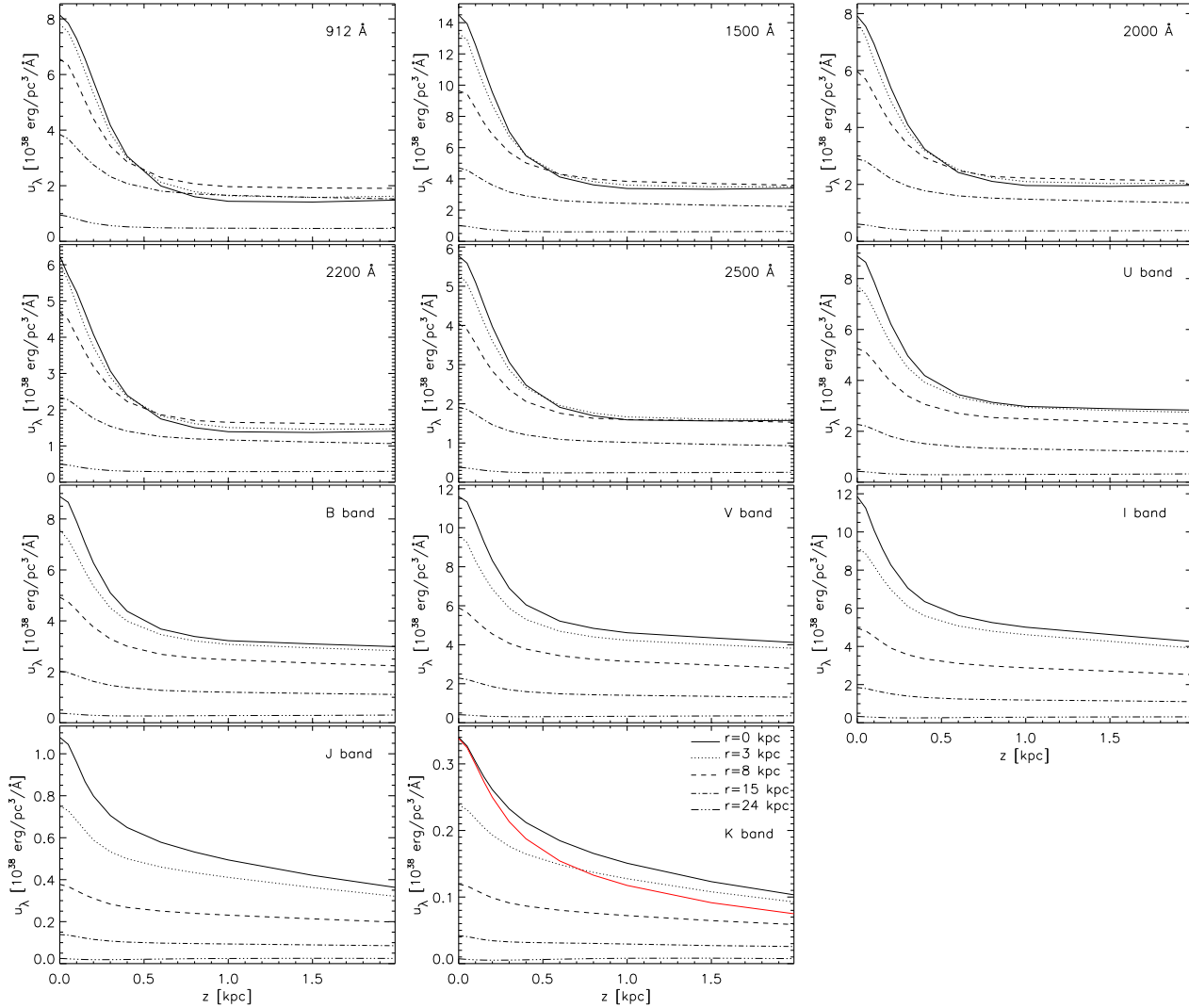


**Figure 5.** Vertical profiles of unit radiation fields from the *thin disk*, for  $\tau_B^f = 3.5$ . The solid line represents the profiles going through the centre ( $R = 0$  pc) while the other lines (see legend) represent profiles at different radial distances from the plane ( $R = 3, 8, 15$  and  $24$  kpc). The different panels show profiles at different wavebands, from the UV to the NIR. The profiles at different wavebands have been scaled as in Fig. 4. The profile overplotted with the red line in the bottom right panel (the K-band case) represents the dustless solution.

length, by a factor 0.016 in our model). When the horizon gets so big that new geometrical components in emissivity and/or opacity enter into the horizon ellipsoid, and these new geometrical components have a different ratio  $\eta/\kappa$  than the ratio at  $z = 0$ , Eq. 6 will break down. This happens beyond a certain galactocentric radius, where the height of the horizon ellipsoid becomes larger than the scale-height of the thin disk. Then the spatial variation of total opacity in  $z$  within the horizon ellipsoid is no longer well approximated by the spatial variation in opacity of dust belonging to the thin disk. This is due to the dust opacity from the thick dust disk (which has a larger scale height than that of the stellar emissivity in the thin disk). Thus, according to Eq. D22, the RFs will start to fall off from the maximum value reached in the (completely) optically thick case (Eq. D23), explaining the reduction in the mid-plane RFs in the outer disk. Eventually the RFs will tend towards an inverse square law decrease, which sets in at radii beyond which all outwards lines of sight (in the plane as well as perpendicular to the plane) become optically thin.

iii) *Intermediate cases;  $z = 0$ .* At longer UV/shorter optical

wavelengths, the profiles show a mixed behaviour, between the optically thin and optically thick limits. Essentially they resemble the profiles from the optically thick cases, with the difference that the flat part in the inner radius is missing. This is due to the fact that already in the inner region the horizon surface is given by a prolate ellipsoid and not by a sphere. Because the height of this ellipsoid is always significantly larger than the scale-height of the thin stellar disk and increases progressively with increasing radius, there is a corresponding decrease in the ratio of stellar emissivity to dust opacity (in vertical direction), resulting in the monotonic decrease of the RFs.

Secondly, we describe the behaviour of the radial profiles at various vertical distances from the plane.

i) *The optically thin case; high  $z$ .* As before, this arises at longer optical wavelengths. The profiles show a similar behavior to the radial profiles in the plane of the disk, but with a shallower decrease. This happens because the fractional change in the distances to all emitting elements is smaller from an outside view than from an inside view (within the disk).



ii) The optically thick case; high  $z$ . The profiles at large vertical distance are rather flat, as seen in Fig. 4 in the UV range at  $z = 1 - 2$  kpc. This qualitative change in the solution for high  $z$  is because the thick dust disk, rather than the thin dust disk, controls the emission escaping from the thin disk. Even from a vantage point 2 kpc above the disk (the maximum height calculated here), the thin stellar disk is viewed through an optically thick layer of dust in the thick disk extending over almost  $2\pi$  sterad. The level of the energy densities of the RF is determined by the ratio of thin disk emissivity to thick disk  $\kappa$  at the depth of the emitting surface<sup>2</sup> from which the escaping photons are emitted. Because of the much steeper  $z$  dependence of the thin disk emissivity compared to that of the thick dust disk opacity, this depth is well below the  $\tau = 1$  surface (as seen from above)- ie the effective line-of-sight optical depth to the emitting surface is  $> 1$ . This in turn means that the emitting surface has a larger extent than the extent of the  $\tau = 1$  surface as seen from  $z = 0$ , explaining the much flatter form of the RF curve with radius for the  $z = 2$  kpc case compared to the  $z = 0$  kpc case.

### 5.1.2 The vertical profiles

The trends in the vertical profiles can be easily explained following the trends already discussed for the radial profiles. Thus, at shorter wavelengths, where the disks are optically thick, the profiles in the centre ( $R = 0$ ) show a decrease in the energy density with increasing  $z$ , until a certain distance above the disk, from where the RF remain fairly constant (see Fig. 5). As discussed for the radial profiles, in an optically thick case, the RF vary according to Eq. 6, as long as the vantage point is within the dust layer. However, unlike the radial variation, in the vertical direction the RFs are affected by the two dust disk structure, where the disk opacity has a different variation from that of the stellar emissivity. The RFs will therefore decrease with increasing vertical distance from the disk, and this behavior continues also for vertical profiles at larger radii, since the disk remains optically thick for a large range of radial distances. Moving still further out in  $z$ , it becomes possible for light to freely escape upwards from an emitting surface (below) which marks the transition (in the vertical direction) from optically thick to optically thin. At a vantage point more than 500 pc up, the contribution to the RFs from this surface dominates the in situ contribution from the thin stellar disk, whose emissivity is tiny at more than a few scale heights. Because at short wavelengths the thin disk is optically thick (face-on) over a large range of galactocentric radii, the emitting surface extends over almost  $2\pi$  sterad. Thus, a vantage point at larger vertical distances above the disk will essentially see a constant surface-brightness until large radii, causing the RFs to remain constant higher-up above the disk.

The trend of decreasing the RF with increasing  $z$  followed by a flat trend with  $z$  is gradually changing from shorter to longer wavelengths, as the disk becomes more optically thin. Eventually in the

<sup>2</sup> When viewing any optically thick emitting body from the outside, the photons that one sees from that body will on average have originated from positions with line-of-sight optical depths to the observer of order unity. For bodies with a strong line of sight gradient in optical depth these positions at which the escaping photons are emitted will be at a rather localised distance from the observer, thus lying on a surface. We call this surface the "emitting surface". The characteristics of the radiation from the emitting surface will be determined by the characteristics of the radiation field in the optically thick layer just below the emission surface, which, in turn, will be determined by the local ratio  $\eta/\kappa$  just below the emission surface.

optically thin case there is only a continuous decrease of the RF with increasing  $z$ . For comparison, the solution with no dust at all is overplotted with a red line in the panel corresponding to the K-band. One can see that the vertical profile calculated for the longer optical wavelengths and for  $\tau_B^f = 3.5$  tends towards the completely optically thin solution, though the latter shows a much steeper decrease with increasing vertical distance.

Coming back to the optical thick cases, but looking at the profiles at larger radii (Fig. 5) one can see a similar behavior to that in the centre of the galaxy. However, at larger vertical distances above the disk, where the energy densities become constant, the overall level of the constant is higher than that of the RF in the centre of the galaxy. So the profiles do not show a monotonic behavior in this respect. This is because, although the vantage point above the disk will also see a constant surface brightness, the level of this is mainly determined by the thin (small scale-height) dust disk, since the thick dust disk (with the larger scale-height) becomes more optically thin. In other words at smaller radii and high  $z$  the radiation fields are equal to

$$u(R) = \frac{\eta(R)}{\kappa_1(R) + \kappa_2(R)} \frac{1}{(1-A)c} \quad (7)$$

while at intermediate radii and high  $z$  the radiation fields are equal to

$$u(R) = \frac{\eta(R)}{\kappa_2(R)} \frac{1}{(1-A)c} \quad (8)$$

where  $\kappa_1$  and  $\kappa_2$  are the local opacities of the thick and thin dust disks, respectively. These are generalisations of Eq. D23, where the mid-plane opacities have been replaced by local opacities. As a consequence, the surface brightness increases at a intermediate radii, since the layer of constant surface brightness moves towards the plane of the disk. There will be a radius at which a maximum in the value of the energy density of the RF at larger  $z$  is attained, after which this will start to slowly decrease again. This causes the non-monotonic behaviour of the radiation fields above the disk with increasing radius. At longer wavelength this never happens, because the thin dust disk becomes transparent even in the inner radii.

## 5.2 The Disk

In our model we consider the disk to be a source of only optical/NIR photons from an older stellar population, with stars old enough to have been dynamically heated to a thicker disk configuration.

At shorter optical wavelengths the radial profiles at  $z = 0$  are rather flat (see Fig. 6). This behaviour is quite different from that of the thin disk at the same wavelengths (see Fig. 4) and appears because the stellar disk has a larger scale-height than that of the thin stellar disk. Thus, as in the thin disk case, at small radii and at  $z = 0$  the disk is optically thick in the radial direction and more optically thin in the vertical direction. Thus the horizon surface is given by a prolate ellipsoid. Although the height of this ellipsoid continuously increases with radius (as in the case of the thin disk), this still remains smaller than the scale-height of the stellar disk. So, unlike the thin disk case at shorter optical wavelength (e.g. B band), the ratio between stellar emissivity to dust opacity will remain fairly constant within the galactocentric radius for which the height of the ellipsoid is smaller than the scale-height of the stellar disk. Therefore, radial profiles for the radiation fields are flatter in the inner disk.

At larger radii though, the disk become optically thin, consis-

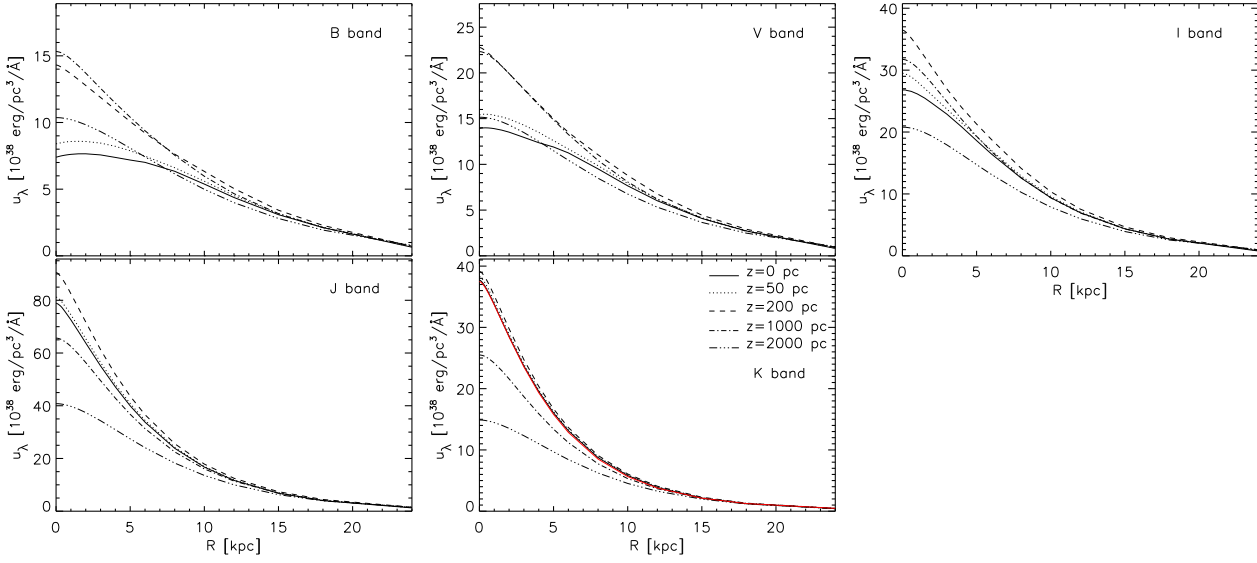


**Figure 6.** Radial profiles of unit radiation fields from the **disk**, for  $\tau_B^f = 3.5$ . The solid line represents the profiles in the plane ( $z = 0$  pc) while the other lines (see legend) represent profiles at different vertical distance from the plane ( $z = 50, 200, 1000$  and  $2000$  pc). The different panels show profiles at different wavebands, from the B band to the NIR. The profile overplotted in red in the bottom right panel (the K-band case) represents the dustless solution scaled to the  $\tau_B^f = 3.5$  solution.

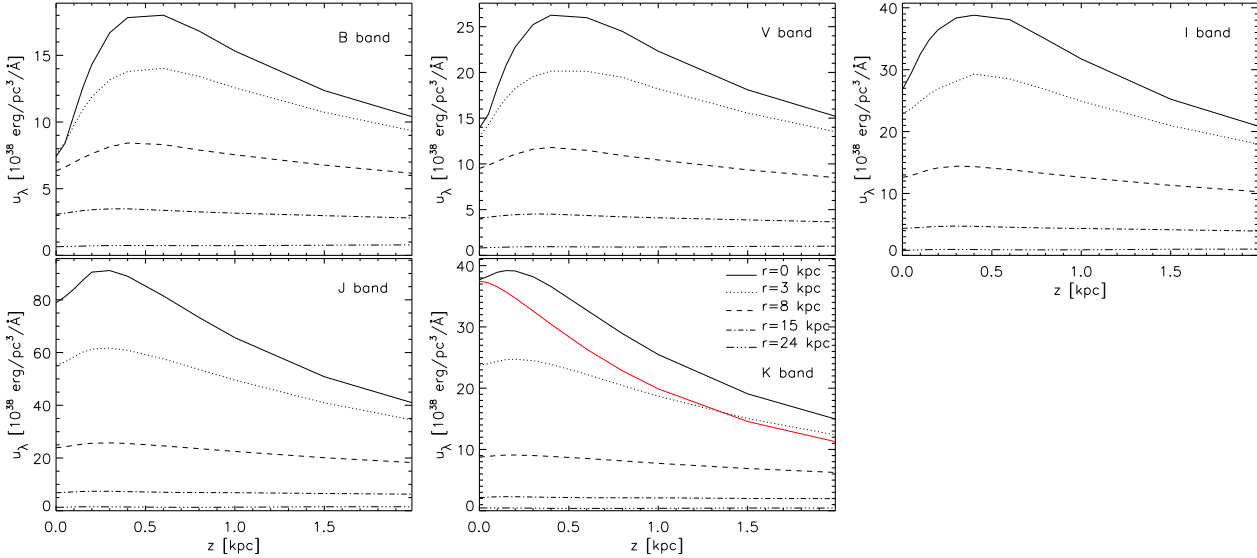


**Figure 7.** Vertical profiles of unit radiation fields from the **disk**, for  $\tau_B^f = 3.5$ . The solid line represents the profiles going through the centre ( $R = 0$  pc) while the other lines (see legend) represent profiles at different radial distance from the plane ( $R = 3, 8, 15$  and  $24$  kpc). The different panels show profiles at different wavebands, from the B band to the NIR. The profile overplotted in red in the bottom right panel (the K-band case) represents the dustless solution.

tent with a radial profile of RF decreasing with increasing radius. At longer optical/NIR wavelengths, the disk becomes optically thin even in the inner part, therefore the RF will show a continuous decrease with increasing radius. For comparison, the solution with no dust at all is overplotted with a red line in the panel for the K-band. One can see that the radial profile calculated for the longer optical wavelengths and for  $\tau_B^f = 3.5$  is very well described by the completely optically thin solution.

The behavior of the RFs above the disk can be better seen in the vertical profiles (see Fig. 7). The dominant feature of these profiles is the existence of a maximum in the energy density of the RFs at an intermediate distance above the plane. Thus, the RFs in-

crease from  $z = 0$  until a certain height, and then they decrease again. This is because the stellar emissivity in the disk has a larger scaleheight than the scaleheight of both dust disks. So in the optically thick regime the energy density of the RFs goes up until the solution for the optically thin case is reached. The height for which the maximum is obtained decreases continuously with increasing optical wavelength (due to the decrease in the optical thickness of the disk). In the K-band the maximum is obtained at very small distances above the plane, but it never reaches the  $z = 0$  plane. This shows that the completely optically thin solution is approached, but still not reached. The dustless case (the red profile in Fig. 7) indeed shows a maximum at  $z = 0$ .

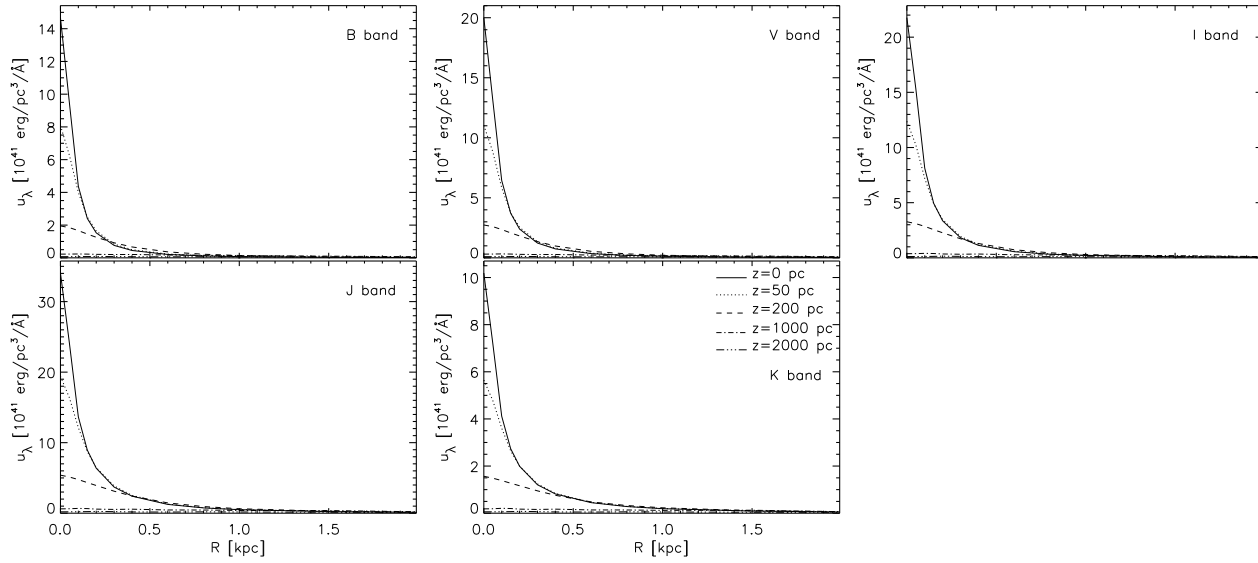


**Figure 8.** Radial profiles of unit radiation fields from the **bulge**, for  $\tau_B^f = 3.5$ . The solid line represents the profiles in the plane ( $z = 0$  pc) while the other lines (see legend) represent profiles at different vertical distances from the plane ( $z = 50, 200, 1000$  and  $2000$  pc). The different panels show profiles at different wavebands, from the B-band to the NIR. The calculations are for de Vaucouleurs bulges.

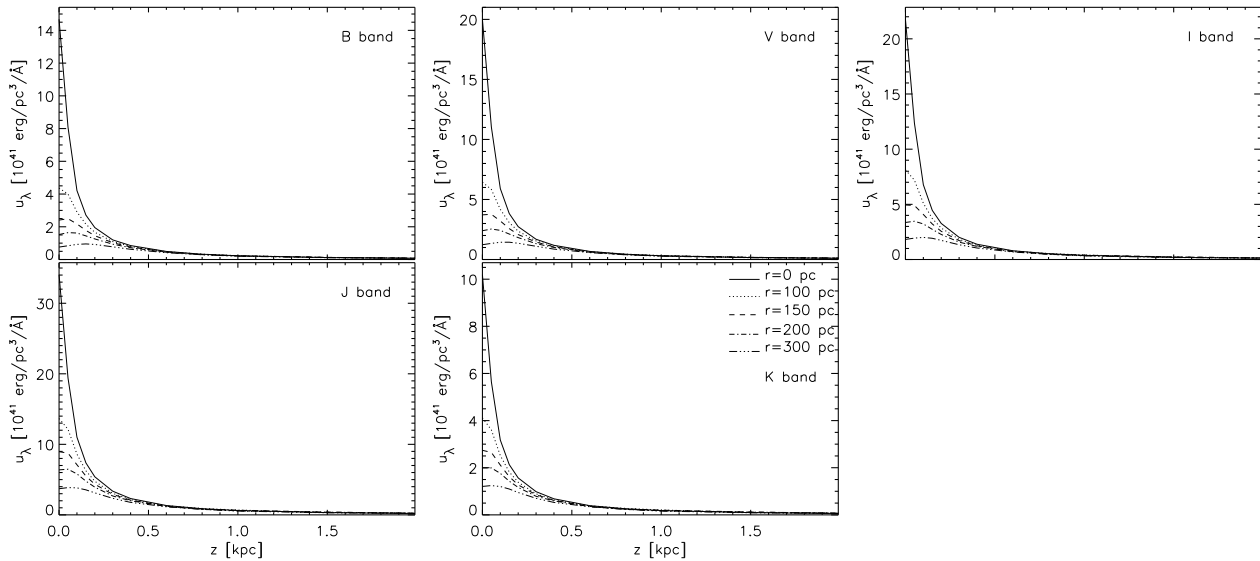


**Figure 9.** Vertical profiles of unit radiation fields from the **bulge**, for  $\tau_B^f = 3.5$ . The solid line represents the profiles going through the centre ( $R = 0$  pc) while the other lines (see legend) represent profiles at different radial distance from the plane ( $R = 3, 8, 15$  and  $24$  kpc). The different panels show profiles at different wavebands, from the B-band to the NIR. The calculations are for de Vaucouleurs bulges.

At larger radii the vertical profiles are very flat in all cases, because the typical distance to the emitting regions, irrespective of whether they are optically thin or optically thick, does not change much.

### 5.3 The Bulge

Here we discuss the spatial trends of radiation fields for de Vaucouleurs bulges (corresponding to a Sérsic index  $n = 4$ ). Deviations from these trends in bulges with different Sérsic indices will be discussed in Sect. 7. Unlike the disk, the RFs of the bulge in the plane of the disk ( $z = 0$ ) and for the optically thick cases (e.g. B band) do not show a constant trend with radial distance, even for the most op-

tically thick cases (see Fig. 8). On the contrary, the radial profiles show a very steep decrease at small radii. This is because of the steep dependence of stellar emissivity on radius, always ensuring a monotonic decrease in the ratio of stellar emissivity to dust opacity. By the same token, the same trend can be seen in the vertical profiles at  $R = 0$  (see Fig. 9).

However, going away from the centre, the vertical profiles start to qualitatively resemble the behaviour of the disk (a maximum in the energy densities at an intermediate distance above the plane). This is because the bulge has, like the disk, a layer of stellar emissivity going above the dust layer, namely an effective radius that is larger than the scale-height of the dust disks. Consequently, there is also a non-monotonic behavior in the radial profiles

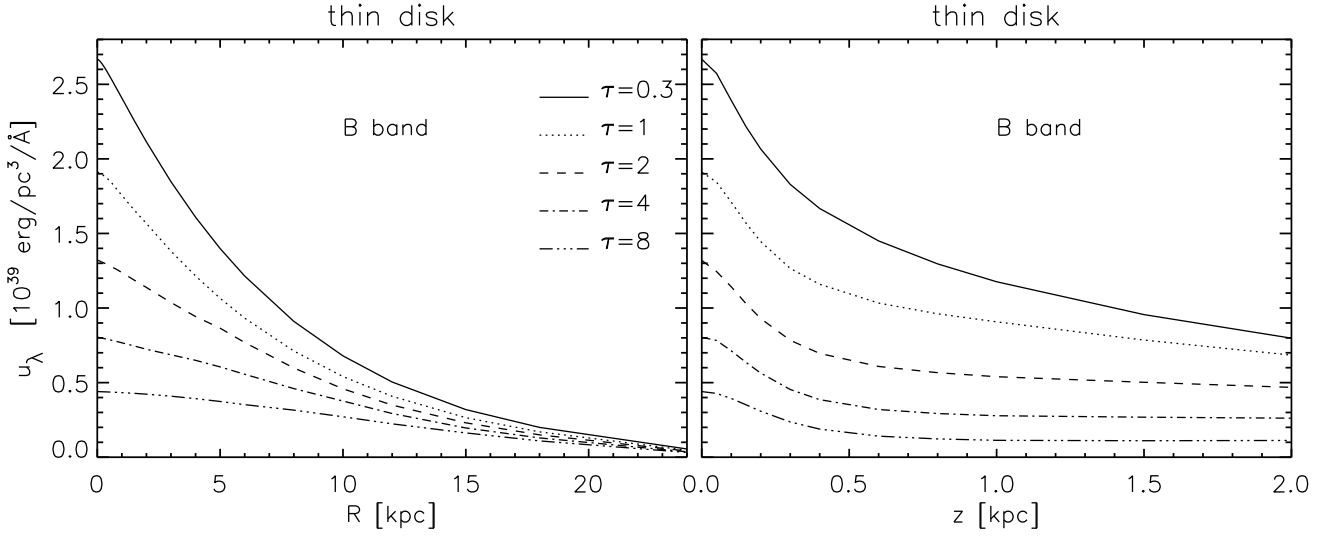


**Figure 10.** Left: B band radial profiles of unit radiation fields from the **thin disk** calculated in the plane ( $z = 0$  pc). Right: Corresponding vertical profiles calculated through the centre ( $R = 0$  pc). The different lines represent profiles corresponding to different central face-on dust opacities in the B-band  $\tau_B^f$  (see legend).

files at larger vertical distances, as in the case of the disk. At larger  $R$  and  $z$  the RF tend to an inverse square law.

## 6 VARIATION OF RADIATION FIELDS WITH CENTRAL FACE-ON DUST OPACITY $\tau_B^f$

### 6.1 The Thin Disk

The variation of the radiation fields of the thin disk with  $\tau_B^f$  is exemplified in Fig. 10, for radial positions in the plane of the disk as well as for vertical positions at  $R = 0$ , for a fixed wavelength (B-band). The first characteristic of the curves is the decrease of the energy density of the RF with increasing  $\tau_B^f$ . This is to be expected, as photons coming from a wider range of distances can reach any given vantage point in the galaxy in the optically thin case than in the optically thick case.

The radial profiles (left panel Fig. 10) also show the expected trend with optical thickness, namely the change from a continuously decreasing energy density of the RF with increasing radius for optically thin cases, to, for optically thick cases, a profile which is almost flat in the inner regions, only markedly decreasing at high increasing radii. (see detailed explanations in Subsect. 5.1.1). This is similar with the trend with wavelength for the same spatial locations (see Fig. 4), since the increase in wavelength is followed by a decrease in the dust opacity at that wavelength.

The vertical profiles (right panel Fig. 10) show a transition from a continuously decreasing energy density of the RF with increasing vertical distance from the plane in the optically thin case, to, for optically thick cases, profiles which also decrease at smaller distances above the plane, but become flat at higher vertical positions. This is the expected trend when moving from an optically thin to an optically thick case, as explained in Subsect. 5.1.2 (see also the similar trend with wavelength in Fig. 5).

### 6.2 The disk

As in the case of the thin disk, the radial profiles in the plane of the disk and the vertical profiles in the centre of the disk (given for

the B-band in Fig. 11) show a decrease in the energy density of the radiation fields with increasing dust opacity  $\tau_B^f$ .

The radial profiles for the optically thin cases show a continuous decrease with increasing radius (left panel Fig. 11), since the disk is in these cases optically thin even in the inner regions. In the optically thick cases the radial profiles are flat in the inner radii, or even slightly increase, followed by a decrease of the energy densities at larger radii. The disk remain essentially flat for radial distances for which the disk is still optically thick. This means that the higher the face-on optical depth  $\tau_B^f$ , the larger the radius for which the disk is optically thick, and therefore the profiles are flat.

As discussed in Sec. 5.2, the vertical profiles (right panel Fig. 11) show a maximum in the energy density at intermediate vertical distances, due to the fact that the stellar emissivity in the disk has a larger scaleheight than the scaleheight of the two dust disks. The vertical distance at which this maximum occurs increases with increasing dust opacity  $\tau_B^f$ , since the optical thick regime extends to higher vertical distances in an optical thick case. This effect is particularly strong for the  $\tau_B^f = 8$  case, where the energy densities increase by a factor of  $\sim 6$ , when moving from the centre to a position 600 pc above the plane.

### 6.3 The Bulge

The radiation fields of the bulge also decrease with increasing  $\tau_B^f$ , albeit at a much smaller rate than for the thin disk and disk (see Fig. 12). The radial profiles of RFs in the plane of the disk show a monotonic decrease with increasing radial distance, irrespective of  $\tau_B^f$ . Similarly, the vertical profiles of RFs at  $R = 0$  pc show a monotonic decrease with increasing vertical distance for all dust opacities considered here. As explained in Sect. 5.3, even in the very optically thick cases the profiles show a steep decrease with  $R$  and  $z$  in the central regions due to the very steep dependence of the stellar emissivity with radial and vertical distance.

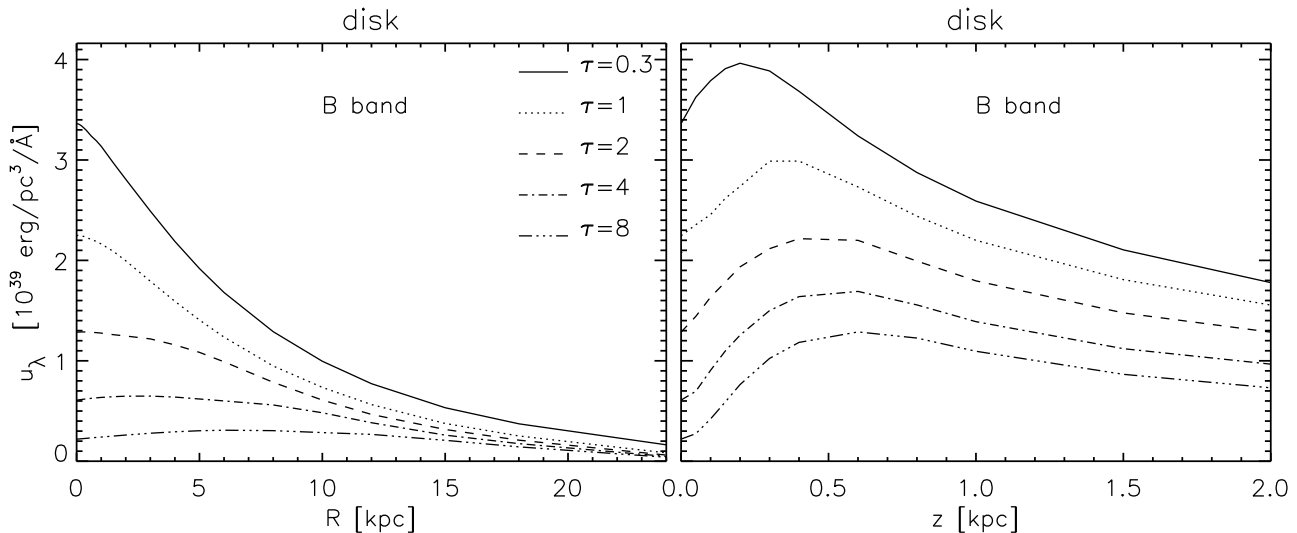


**Figure 11.** Left: B band radial profiles of unit radiation fields from the **disk** calculated in the plane ( $z = 0$  pc). Right: Corresponding vertical profiles calculated through the centre ( $R = 0$  pc). The different lines represent profiles corresponding to different central face-on dust opacities in the B-band  $\tau_B^f$  (see legend).

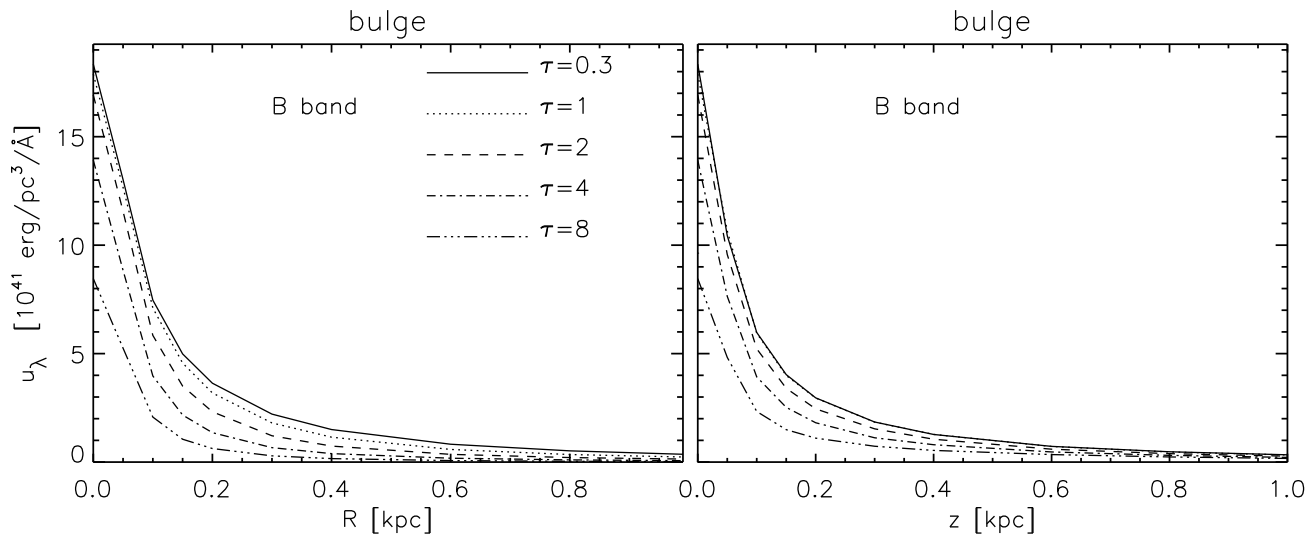


**Figure 12.** Left: B band radial profiles of unit radiation fields from the **bulge** calculated in the plane ( $z = 0$  pc). Right: Corresponding vertical profiles calculated through the centre ( $R = 0$  pc). The different lines represent profiles corresponding to different central face-on dust opacities in the B-band  $\tau_B^f$  (see legend). The calculations are for de Vaucouleurs bulges.

## 7 VARIATION OF RADIATION FIELDS WITH BULGE SÉRSIC INDEX

In Sects. 5.3 and 6.3 we discussed the spatial variation of the radiation fields from bulges, as well as the variation with wavelength and central face-on dust opacity. This was done for the concrete example of de Vaucouleurs bulges. Here we investigate whether the trends seen in the RF for bulges change when different Sérsic indices are considered. In Fig. 13 we show radial and vertical profiles of RFs at  $z = 0$  and  $R = 0$  respectively, for four different values of Sérsic indices,  $n = 1, 2, 4, 8$ , for the case  $\tau_B^f = 3.5$ , and for the B-band.

The radial profiles show a monotonic decrease with increasing radial distance, irrespective of the Sérsic index. However, for higher Sérsic indices the decrease is steeper, in particular in the very central regions, as expected due to the steeper dependence of

the stellar emissivity. For  $n = 1$  the profiles start to resemble those from the disk, due to the exponential form of the stellar emissivity.

The vertical profiles show more pronounced differences in the trends for the different Sérsic indices. Thus, for lower Sérsic index the profiles become less steep. In the extreme case of  $n = 1$  the profile not only flattens, but even shows a second maximum. This exponential form of the stellar emissivity produces a solution closer to the disk solution, where a maximum occurs at a certain vertical distance from the disk. This is due to the fact that the stellar emissivity has a larger scale-height than that of the two dust disks. However, unlike the disk, there is another maximum in the plane of the disk. This is because, although the stellar emissivity is described by an exponential distribution, this emissivity is spatially distributed in an ellipsoid rather than a disk.

Overall we can conclude that the radiation fields from bulges strongly depend on the assumed Sérsic index of the bulge. Because

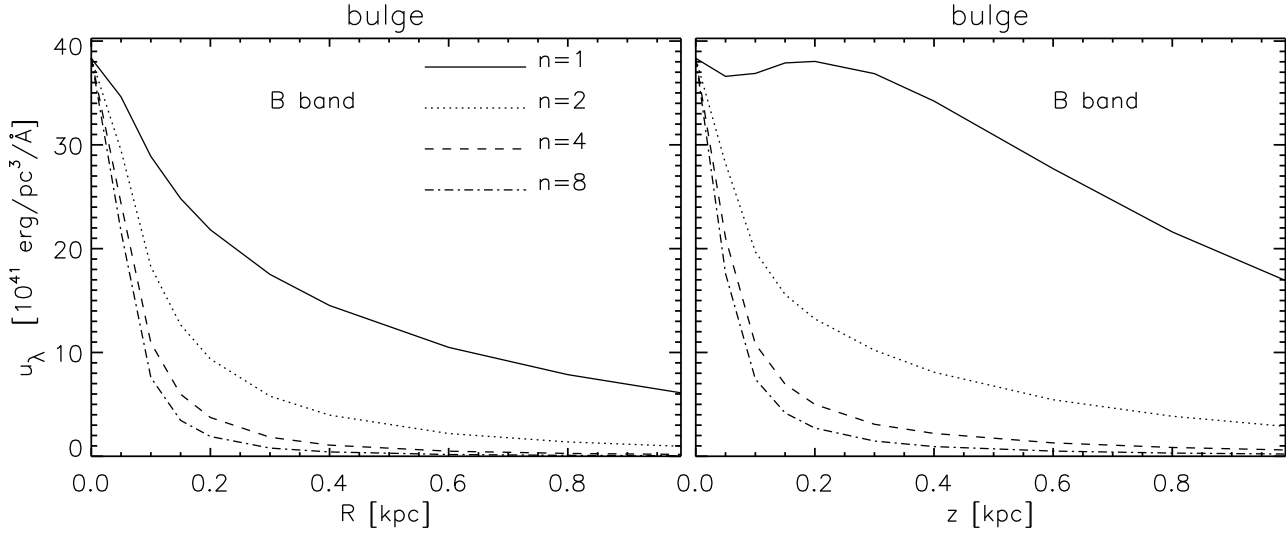


**Figure 13.** Left: B band radial profiles of unit radiation fields from the **bulge** calculated in the plane ( $z = 0$  pc). Right: B band vertical profiles from the bulge calculated through the centre ( $R = 0$  pc). The different lines represent profiles corresponding to different Sérsic indices of the stellar emissivity (see legend). The profiles are scaled such that the maximum of the energy density of the radiation fields of a model galaxy reaches the value of  $38.34 \times 10^{41}$ , which is the maximum intensity for the model with  $n = 8$ . The calculations are for  $\tau_B^f = 4.0$ .

of this we include in the library of radiation fields for bulges the calculations for all four values of Sérsic indices shown above.

**8 APPLICATION: THE EFFECT OF DIFFERENT BULGE SÉRSIC INDICES ON DUST HEATING**

One important conclusion of this study is that the radiation fields from bulges strongly depend on the value of the Sérsic index of the stellar emissivity (see Sect. 7). This raises the possibility that the heating of dust in the disk may also be strongly influenced by the type of bulge a galaxy would host.

Indeed, when plotting the SED of the radiation fields (normalised to the local interstellar radiation fields - LIRF - Mathis et al. 1983), in the centre of the bulge (Fig. 14), one can see a substantial increase in the energy densities from an  $n = 1$  case to an  $n = 8$  case. Without any explicit calculation of the dust heating, this already indicates that the temperature of the dust heated by radiation fields coming from bulges with different Sérsic indices will change significantly.

To check this effect we used the codes from Popescu et al. (2011) to perform calculations for dust heating and emission for a model galaxy having bulges described by different Sérsic indices ( $n = 1, 2, 4, 8$ ). We chose a typical value for the bulge-to-disk ratio, of  $B/D = 0.33$ . We also considered a galaxy having the unit luminosities (as described in our model - see Sect. 3 and Popescu et al. 2011) for the old and young stellar populations ( $SFR = 1 M_\odot/\text{yr}$ ,  $old = 1$ ) and  $\tau_B^f = 4.0$ . The resulting integrated SEDs are shown in the top panel of Fig. 15. One can see that with higher the Sérsic index, the larger the emission in the 24 to 60  $\mu\text{m}$  wavelengths range is. This is because of the very strong heating of the dust in the very central region of the disk by optical photons emitted by the bulge. Although the total dust luminosity is almost unaffected by the shift in the Sérsic index, the integrated mid-infrared/far-infrared colours are somewhat boosted for galaxies containing bulges with high Sérsic index. This boost in colour is however moderate in comparison with the boost due to an increase in the  $B/D$  ratio, as shown in Fig. 19 of Popescu et al. (2011).

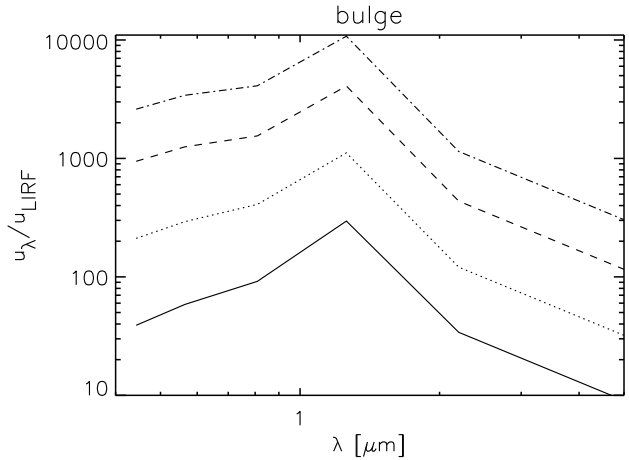


**Figure 14.** The SED of the unit radiation fields (normalised to the LIRF) at  $R = 0$  kpc and  $z = 0$  kpc, for bulges having different Sérsic indices of the stellar emissivity (plotted with different lines; legend as in Fig. 13)

The stronger effect though appears in the surface-brightness distribution, in particular in the central regions of galaxies containing bulges. In the bottom panel of Fig. 15, one can see that the radial profiles of galaxies containing bulges described by different Sérsic indices can vary by a factor of more than 10 at 24  $\mu\text{m}$ . This is remarkable, since dust emission at 24  $\mu\text{m}$  is commonly interpreted in terms of heating either by UV photons in star-formation regions or from accretion sources (AGN), whereas here the heating is dominated by old stars in the bulge. Moreover, one can see that this enhancement occurs only within a few hundred parsec of the centre. At these linear scales, for resolved galaxies beyond 10 Mpc the excess emission due to the bulge heating will appear as a separate warm point-like source at the angular resolution of the Spitzer Space Telescope at 24  $\mu\text{m}$ . Particular care must therefore be taken in interpreting central sources seen in the mid-infrared towards spiral galaxies with bulges, to distinguish between an obscured low-

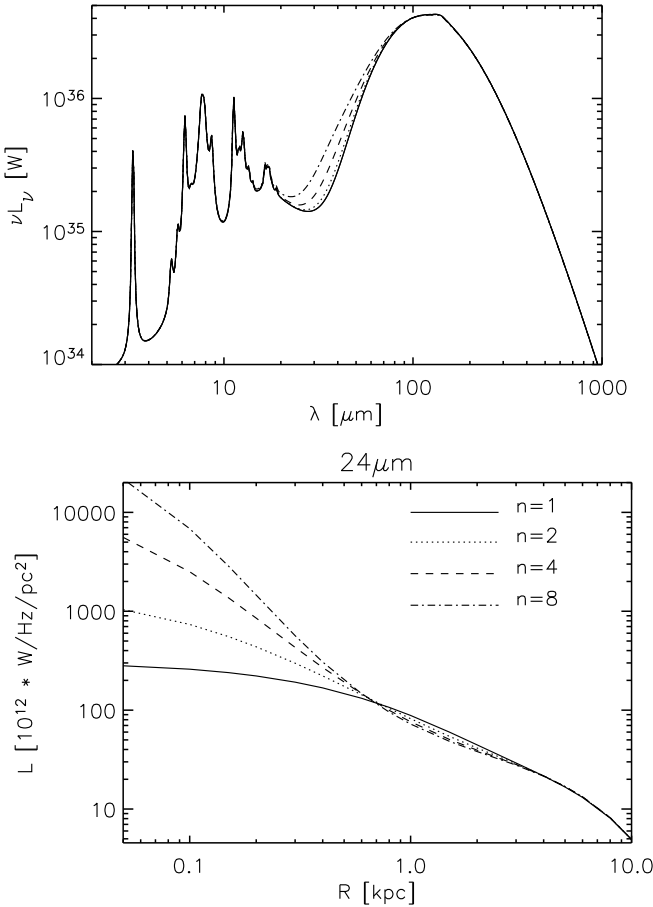


**Figure 15.** Spatially integrated diffuse dust emission SEDs (top) and  $24\mu\text{m}$  radial profiles along the major-axis (bottom) of a model galaxy (containing a young stellar disk, an old stellar disk - with a B-band exponential scale-length of 5.67 kpc - and a bulge with  $R^{eff} = 1.3$  kpc). The parameters of the model were set to  $SFR = 1 M_\odot/\text{yr}$ ,  $old = 1$ ,  $\tau_B^f = 4.0$ ,  $B/D = 0.33$ . The different lines correspond to different Sérsic indices of the stellar emissivity in the bulge (see legend). The profiles are for a galaxy seen face-on.

luminosity AGN, star-formation activity and the effect of the bulge we have identified here.

## 9 SUMMARY

In this paper we provide a library of energy densities of the diffuse radiation fields arising from stars in the main morphological components of spiral galaxies: disks, thin disks and bulges. The library contains 630 two-dimensional spatial grids (in cylindrical coordinates) of energy densities of the RFs, spanning seven values of face-on central optical depth  $\tau_B^f$ , 15 values of wavelength, and, for bulge RFs, four values of Sérsic index  $n$ . Thus, we considered  $\tau_B^f = 0.1, 0.3, 0.5, 1.0, 2.0, 4.0, 8.0$ ,  $n = 1, 2, 4, 8$  and wavelengths from  $912 \text{ \AA}$  to  $5 \mu\text{m}$ . The radiation fields are sampled on an irregular grid with sampling intervals in the radial direction ranging from 50 pc in the centre to up to 2 kpc in the outer disk and in the vertical direction ranging from 50 pc in the plane to up to 500 pc in the outer halo.

The model radiation fields are those used to generate the large

library of dust- and PAH-emission SEDs presented in Popescu et al. (2011). This library is self-consistently calculated with the corresponding library of dust attenuations first presented in Tuffs et al. (2004) and then in updated form in Popescu et al. (2011). All calculations were made using a modified version of the ray-tracing radiative transfer code of Kylafis & Bahcall (1987), and the dust model from Weingartner & Draine (2001) and Draine & Li (2007), incorporating a mixture of silicates, graphites and PAH molecules.

We discussed the radial and vertical variation of the RFs, as well as their variation with  $\tau_B^f$ , and, for bulges, with the Sérsic index. We give analytic formulae for the radiation fields of a dust-less stellar disk, as well as for a stellar disk with one and with two dust disks. We use these to explain the trends in the profiles of the thin disk. We also show how the library can be self-consistently combined with the results from modelling the spatially integrated UV/optical/submm SEDs of galaxies from Popescu et al. (2011).

As a practical application we calculated the dust emission SEDs for galaxies having different bulge Sérsic indices. We find strong mid-infrared localised emission in the central regions of disks with high Sérsic index bulges, which can mimic a central star-formation region or a mild AGN activity. Unlike these latter two cases, the dust is in this case heated by optical photons from the bulge.

## 10 ACKNOWLEDGEMENTS

We would like to thank the referee, Simone Bianchi, for his very insightful and constructive comments, and in particular for encouraging us to provide the analytic solutions.

## REFERENCES

- Aharonian, F.A. & Atoyan, A.M. 1981, *Ap&SS* 79, 321  
 Aharonian, F.A. & Ambartsumyan, A.S. 1985, *Astrophysics* 23, 650  
 Baes, M., Fritz, J., Gadotti, D.A. et al. 2010, *A&A* 518, L39  
 Baes, M., Verstappen, J., De Looze, I. et al. 2011, *ApJS* 196, 22  
 Bennett C. L. et al., 1994, *ApJ*, 434, 587  
 Bianchi, S. 2008, *A&A*, 490, 461  
 Blumenthal, G.R. & Gould, R.J. 1970, *Rev. Mod. Phys.* 42, 237  
 Brunetti, G. 2000, *Astropart. Phys.* 13, 107  
 Crawford M.K., Genzel, R., Townes, C.H., Watson, D.M. 1985, *ApJ* 291, 755  
 Dermer, C.D. & Atoyan, A.M. 2002, *ApJ*, 568, L81  
 Driver, S.P., Popescu, C.C., Tuffs, R.J., et al. 2007, *MNRAS* 379, 1022  
 de Avillez, M.A. & Breitschwerdt, D. 2007, *ApJL* 665, 35  
 de Looze, I., Baes, M., Bendo, G. et al. 2012a, *MNRAS* 427, 2797  
 de Looze, I., Baes, M., Fritz, J. & Verstappen, J. 2012b, *MNRAS* 419, 895  
 Draine, B.T. & Li, A. 2007, *ApJ*, 657, 810  
 Driver, S.P., Popescu, C.C., Tuffs, R.J. et al. 2007, *MNRAS* 379, 1022  
 Efstathiou, A., Rowan-Robinson, M. & Siebenmorgen, R. 2000, *MNRAS* 313, 734  
 Efstathiou, A. & Rowan-Robinson, M. 2003, *MNRAS* 343, 322  
 Grootes, M., Tuffs, R.J., Popescu, C.C. et al. 2013, *ApJ* 766, 59  
 Hollenbach D.J., Takahashi T., Tielens A.G.G.M. 1991, *ApJ*, 377, 192  
 Israel, F.P. & Maloney, P.R. 2011, *A&A* 531, 19  
 Jones, F.C. 1968, *Phys. Rev* 167, 1159  
 Khangulyan, D. & Aharonian, F. 2005, in *AIP Conf. Proc.* 745, High Energy Gamma-Ray Astronomy, eds. F. A. Aharonian, H. J. Völk, & D. Horns (Melville, NY: AIP), 359  
 Kylafis, N. D. & Bahcall, J. N. 1987, *ApJ*, 317, 637  
 Kylafis, N.D. & Xilouris, E.M. 2005, in “The Spectral Energy Distributions of Gas-Rich Galaxies: Confronting Models with Data”, eds. C.C. Popescu & R.J. Tuffs, *AIPC* 761, 3

- Kusunose, M., & Takahara, F. 2005, ApJ, 621, 285  
 Leboutellier, V., Cormier, D., Madden, S.C. et al. 2012, A&A 548, 91  
 MacLachlan, J.M., Matthews, L.D., Wood, K. & Gallagher, J.S. 2011, ApJ 741, 6  
 Madden S.C., Geis, N., Geuzel R., Herrmann F., Jackson J., Poylitsch A., Stacey G.J., Townes C.H. 1993, ApJ, 407, 579  
 Mathis, J.S., Mezger, P.G., Panagia, N. 1983, A&A 128, 212  
 Misiriotis, A., Popescu, C.C., Tuffs, R.J., & Kylafis, N.D. 2001, A&A, 372, 775  
 Moderski, R., Sikora, M., Coppi, P.S., & Aharonian, F. 2005, MNRAS, 363, 954  
 Möllenhoff, C., Popescu, C. C., Tuffs, R. J. 2006, A&A 456, 941  
 Moskalenko, I.V., Porter, T.A. & Strong, A.W. 2006, ApJ 640, 155  
 Narginen, D.I. & Putanen, J. 1993, A&A 275, 325  
 Pastrav, B.A., Popescu, C.C., Tuffs, R.J., Sansom, A.E 2013a, A&A 553, 80  
 Pastrav, B.A., Popescu, C.C., Tuffs, R.J., Sansom, A.E 2013b, A&A in press (arXiv1308.0458)  
 Pierini, D., Leech, K.J., Tuffs, R.J. & Völk, H.J. 1999, MNRAS 303, 29  
 Pierini, D., Lequeux, J., Boselli, A., Leech, K.J., Völk, H.J. 2001, A&A 373, 827  
 Popescu, C.C. & Tuffs, R.J. 2010, AIPC 1240, 35  
 Popescu, C.C., Misiriotis, A., Kylafis, N.D., Tuffs, R.J. & Fischera, J., 2000, A&A 362, 138  
 Popescu, C.C., Tuffs, R.J., Kylafis, N.D., & Madore, B.F. 2004, A&A 414, 45  
 Popescu, C.C., Tuffs, R.J., Dopita, M.A. et al. 2011, A&A 527, A109  
 Rowan-Robinson, M. 1992, MNRAS 258, 787  
 Rowan-Robinson, M. 2012, IAUS 284, p. 446  
 Rowan-Robinson, M. & Crawford, J. 1989, MNRAS 238, 523  
 Rowan-Robinson, M. & Efstathiou, A. 2009, MNRAS 399, 615  
 Rubin, D., Hony, S., Madden, S.C. et al. 2009, A&A 494, 647  
 Sazonov, S.Y. & Sunyaev, R.A. 2000, ApJ 543, 28  
 Schechtman-Rook, A., Bershad, M.A. & Wood, K. 2012, ApJ 746, 70  
 Siebenmorgen, R. & Krügel, E., A&A 461, 445, (2007)  
 Stawarz, L., Aharonian, F., Wagner, S., & Ostrowski, M. 2006, MNRAS, 371, 1705  
 Stawarz, L., Petrosian, V., & Blandford, R. D. 2010, ApJ, 710, 236  
 Stecker, F.W., de Jager, O.C. & Salamon, M.H. 1992, ApJL 390, 49  
 Tielens, A.G.G.M. & Hollenbach, D. 1985, ApJ 291, 722  
 Tuffs, R. J., Popescu, C. C., Völk, H. J., Kylafis, N. D., Dopita, M. A. 2004, A&A 419, 821  
 Weingartner, J.C. & Draine, B.T. 2001, ApJ, 548, 296  
 Wolfire, M.G., Hollenbach, D. & Tielens, A.G.G.M. 1989, ApJ 344, 770  
 Zdziarski, A.A. 1989, ApJ, 342, 1108

#### APPENDIX A: DERIVATION OF AN ANALYTIC SOLUTION FOR RADIATION FIELDS IN THE MID-PLANE OF AN AZIMUTHALLY SYMMETRIC INFINITELY THIN DUSTLESS STELLAR DISK

We take the stellar disk to be infinitely thin. The contribution to the radiation field at a point P in the disk due to an emitting element in an annulus of the disk at coordinates  $(R', \theta')$  is:

$$du^\theta = \frac{\sigma R' d\theta' \Delta R'}{4\pi R''^2 c} \quad (\text{A1})$$

where  $\sigma(R')$  is the surface density of luminosity,  $R$  is the galactocentric radius of the point P,  $R'$  is the galactocentric radius of the annulus considered,  $R''$  is the offset of P from the emitting element in the annulus,  $\theta'$  is the azimuthal offset of the emitting element with respect to P, and  $c$  is the speed of light. This geometry is illustrated for the cases that P is interior to the annulus in Fig. A1. It should be noted that this expression in Eq. A1 applies to both these

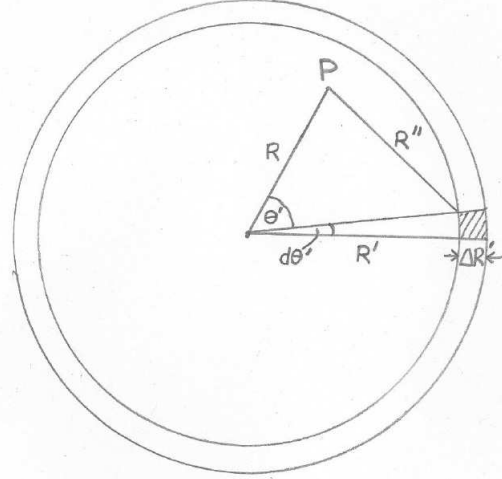


**Figure A1.** Schematic representation of the geometry considered for the calculation of the radiation fields at a point P, with galactocentric radius  $R$ , in an infinitely thin dustless stellar disk due to emitters in an annulus at galactocentric radius  $R'$ . The figure depicts the face-on view point.

cases. The contribution to the radiation field at P from the entire annulus is then:

$$du^{ann} = \int_0^{2\pi} du^\theta d\theta = \frac{\sigma R' \Delta R'}{4\pi c} \int_0^{2\pi} \frac{d\theta'}{R''^2} \quad (\text{A2})$$

Applying the cosine rule:

$$R''^2 = R^2 + R'^2 - 2RR' \cos(\theta') \quad (\text{A3})$$

we obtain:

$$du^{ann} = \frac{\sigma R' \Delta R'}{4\pi c} \frac{1}{R^2 + R'^2} I \quad (\text{A4})$$

where

$$I = \int_0^{2\pi} \frac{d\theta'}{1 - \frac{2RR' \cos(\theta')}{R^2 + R'^2}} \quad (\text{A5})$$

Applying the notation:

$$\beta = \frac{2RR'}{R^2 + R'^2} \quad (\text{A6})$$

the integral in Eq. A5 becomes:

$$I = \int_0^{2\pi} \frac{d\theta'}{1 - \beta \cos(\theta')} \quad (\text{A7})$$

which has the solution

$$I = \frac{4}{\sqrt{1 - \beta^2}} I' \quad (\text{A8})$$

where

$$I' = 2 \tan^{-1} \left( \frac{1 + \beta}{1 - \beta} \right)^{1/2} - \tan^{-1} \frac{\beta}{\sqrt{1 - \beta^2}} = \frac{\pi}{2} \quad (\text{A9})$$

Substituting Eqs. A9, A8 and A6 in Eq. A4 we obtain:

$$du^{ann} = \frac{\sigma R' \Delta R'}{2c} \frac{1}{|R^2 - R'^2|} \quad (\text{A10})$$

This solution applies both for annuli exterior to P (case  $R' > R$ ) and for annuli interior to P (case  $R' < R$ ). To obtain the total radiation



field at P we integrate over  $R'$ , splitting the integration about the singularity at  $R = R'$ :

$$u(R) = u_1(R) + u_2(R) \quad (\text{A11})$$

where

$$u_1(R) = \int_0^R du^{ann} dR' \quad (\text{A12})$$

$$u_2(R) = \int_R^\infty du^{ann} dR' \quad (\text{A13})$$

The result of this integration is:

$$u_1(R) = \frac{1}{4\pi c R^2} \int_0^R f\left(\frac{R'}{R}\right) 2\pi R' \sigma(R') dR' \quad (\text{A14})$$

$$u_2(R) = \frac{1}{4\pi c} \int_R^\infty \frac{f\left(\frac{R'}{R}\right) 2\pi R' \sigma(R') dR'}{R'^2} \quad (\text{A15})$$

where

$$f(\xi) = \frac{1}{1 - \xi^2} \quad (\text{A16})$$

## APPENDIX B: DERIVATION OF AN ANALYTIC SOLUTION FOR RADIATION FIELDS OF AN AZIMUTHALLY SYMMETRIC DUSTLESS STELLAR DISK WITH FINITE THICKNESS

It is straightforward to extend the solutions derived in Appendix A for the radiation fields in the plane of an infinitely thin disk to derive expressions for radiation fields at any position in  $(R, z)$  of a disk which has a finite thickness.

We consider now the annulus in Fig A1 as lying in a plane offset  $z'$  from the plane of the galaxy. The contribution to the radiation field at a point P with cylindrical coordinates  $(R, z)$  due to an emitting element in the annulus at coordinates  $(R', z')$  is then:

$$du^\theta = \frac{\eta R' d\theta' \Delta R' \Delta z}{4\pi R''^2 c} \quad (\text{B1})$$

where  $\eta$  is the volume stellar emissivity,  $\Delta z$  is the thickness of the annulus, and  $R''$  is the offset (in 3D) of the point P from the emitting element in the annulus, where

$$R''^2 = R'^2 + (z' - z)^2 \quad (\text{B2})$$

and  $R''$  is the projection of the vector joining P to the emitting element in the plane of the annulus. Analogous to the solution for the infinitely thin disk (Eq. A2), the contribution to the radiation field at P from the entire annulus is:

$$du^{ann} = \int_0^{2\pi} du^\theta d\theta' \Delta z' = \frac{\eta R' \Delta R'}{4\pi c} \int_0^{2\pi} \frac{d\theta'}{R''^2} \quad (\text{B3})$$

Substituting Eq. B2 for  $R''$ , as given by Eq. A3 (applied in the plane at  $z$ ), we obtain:

$$du^{ann} = \frac{\eta R' \Delta R' \Delta z}{4\pi c} \frac{1}{R^2 + R'^2 + (z' - z)^2} I \quad (\text{B4})$$

where

$$I = \int_0^{2\pi} \frac{d\theta'}{1 - \frac{2RR' \cos(\theta')}{R^2 + R'^2 + (z' - z)^2}} \quad (\text{B5})$$

Applying the notation:

$$\beta = \frac{2RR'}{R^2 + R'^2 + (z' - z)^2} \quad (\text{B6})$$

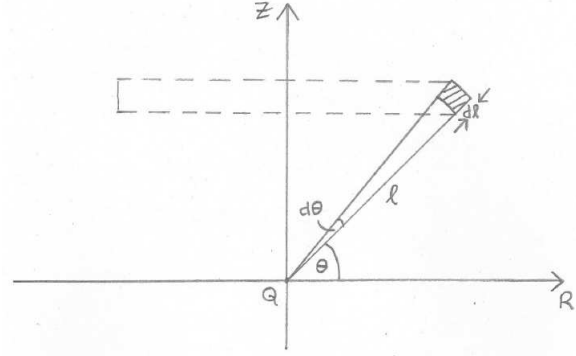


**Figure C1.** Schematic representation of the geometry considered for the calculation of the radiation fields at a point Q in the mid-plane of the disk and at a galactocentric radius of  $R$ . Radiation arriving at Q is emitted from an annulus at distance  $l$ , with angle  $\theta$  subtended at the plane. The polar axis of the annulus passes through Q. The figure depicts the edge-on view point.

we recover the same form for the integral in Eq. B5 as previously obtained in Eq. A7, which has the solution:

$$I = \frac{2\pi}{\sqrt{1 - \beta^2}} \quad (\text{B7})$$

Substituting Eqs. B7 and B6 in Eq. B4 we obtain:

$$du^{ann} = \frac{\eta R' \Delta R' \Delta z'}{2c} g(R, z, R', z') \quad (\text{B8})$$

where

$$g = \frac{1}{|\sqrt{(R + R')^2 + (z' - z)^2} \sqrt{(R' - R)^2 + (z' - z)^2}|} \quad (\text{B9})$$

We note that the expression for  $du^{ann}$ , given by Eqs. B8 and B9 reduces to Eq. A4 for  $z = z' = 0$ .

Integrating over  $R'$  and  $z'$  we obtain a general solution for the radiation field energy density arising from any distribution of stellar emissivity with cylindrical symmetric geometry in the optically thin limit:

$$u(R, z) = \frac{1}{2c} \int_{-\infty}^{\infty} \int_0^{\infty} g(R, z, R', z') R' \eta(R', z') dR' dz' \quad (\text{B10})$$

## APPENDIX C: DERIVATION OF AN ANALYTICAL SOLUTION FOR RADIATION FIELDS IN THE MID-PLANE OF AN AZIMUTHALLY SYMMETRIC STELLAR DISK WITH ONE DUST DISK

We take the stellar and dust disks to be both exponentially stratified (in vertical direction) while having an arbitrary distribution in radial direction. This allows us to write the volume stellar emissivity  $\eta(R, z)$  and the extinction coefficient  $\kappa(R, z)^3$  as:

$$\eta(R, z) = \eta_{z_0}(R) \exp\left(-\frac{z}{z_s}\right) \quad (\text{C1})$$

$$\kappa(R, z) = \kappa_{z_0}(R) \exp\left(-\frac{z}{z_d}\right) \quad (\text{C2})$$

<sup>3</sup> Here we defined the extinction coefficient as the probability of absorption or scattering of a photon per unit length.

where  $z_s$  and  $z_d$  are the scaleheights of the stellar and dust disks, respectively, and  $\eta_{z_0}(R)$  and  $\kappa_{z_0}(R)$  are the mid-plane stellar emissivity and dust opacity.

Our aim is to derive an analytic expression of the radiation fields in the mid-plane of the disk in the optically thick limit. The term optically thick is used in the sense that the terms  $\eta_{z_0}(R)$  and  $\kappa_{z_0}(R)$  are taken to be constants over the typical range in  $R$  that photons contributing to the mid-plane energy density actually travel. This allows the validity of the solution to be maintained even when the disk becomes transparent in the vertical direction, provided that the scale in radius over which the opacity of the dust disk changes is much larger than the scaleheight of the dust disk.

The contribution to the mid-plane energy density due to direct light from stars in a volume element within a thin shell of radius  $(l, l + dl)$ , and angle  $(\theta, \theta + d\theta)$  (see Fig. C1) is

$$\begin{aligned} du &= u(l, \theta) dl d\theta \\ &= \frac{\eta(l) dV}{4\pi l^2 c} \exp(-\tau(l)) \end{aligned} \quad (\text{C3})$$

where

$$dV = 2\pi l^2 \cos(\theta) d\theta dl \quad (\text{C4})$$

$$\eta(l) = \eta_{z_0}(R) \exp\left(-\frac{l \sin(\theta)}{z_s}\right) \quad (\text{C5})$$

$$\begin{aligned} \tau(l) &= \kappa_{z_0}(R) \int_0^l \exp\left(-\frac{l \sin(\theta)}{z_d}\right) dl \\ &= \frac{\kappa_{z_0}(R) z_d}{\sin(\theta)} \left[1 - \exp\left(-\frac{l \sin(\theta)}{z_d}\right)\right] \end{aligned} \quad (\text{C6})$$

We make the notations:

$$\alpha = \frac{\kappa_{z_0}(R) z_d}{\sin(\theta)} \quad (\text{C7})$$

$$\beta = \frac{\sin(\theta)}{z_d} \quad (\text{C8})$$

$$\gamma = \frac{\sin(\theta)}{z_s} \quad (\text{C9})$$

Substituting Eqs. C4, C5 and C6 into Eq. C3, using the notations from Eqs. C7, C8 and C9 and integrating over  $dl$  we obtain:

$$\begin{aligned} u_\theta d\theta &= d\theta \int_0^\infty u(l, \theta) dl \\ &= d\theta \frac{\eta_{z_0}(R) \cos(\theta) \exp(-\alpha)}{2c} I(\theta, \alpha, \beta, \gamma) \end{aligned} \quad (\text{C10})$$

where

$$I(\theta, \alpha, \beta, \gamma) = \int_0^\infty \exp(-\gamma l) \exp(\alpha e^{-\beta l}) dl \quad (\text{C11})$$

By further manipulating Eq. C11 we obtain:

$$I(\theta, \alpha, \beta, \gamma) = \frac{\alpha^{-x}}{\beta} I'(\alpha, \beta) \quad (\text{C12})$$

where

$$x = \frac{z_d}{z_s} \quad (\text{C13})$$

$$I' = \int_0^\alpha \xi^{x-1} e^\xi d\xi \quad (\text{C14})$$

The integral defining  $I'$  is analytic if  $x$  is a non-negative integer. The simplest solution is for  $x = 1$ , which corresponds to the dust disk having the same scale-height as the stellar disk. In this case

Eq. C12 becomes:

$$I(\theta, \alpha, \beta, \gamma) = \frac{\exp(\alpha) - 1}{\kappa_{z_0}} \quad (\text{C15})$$

Substituting Eq. C15 into Eq. C10 and integrating over  $\theta$  we obtain the analytic solution for the energy density in the mid-plane due to direct light from stars:

$$\begin{aligned} u_{z_0}^{dl}(R) &= 2 \int_0^{\pi/2} u_\theta d\theta \\ &= \frac{\eta_{z_0}(R)}{\kappa_{z_0}(R) c} [1 - I''(R)] \end{aligned} \quad (\text{C16})$$

where

$$I''(R) = \int_0^{\pi/2} \cos(\theta) \exp\left(-\frac{\kappa_{z_0}(R) z_d}{\sin(\theta)}\right) d\theta \quad (\text{C17})$$

From Eqs. C16 and C17 one sees that for very optically thick solutions, in which the range of photons is small in  $z$  as well as in  $R$ ,  $u_{z_0}^{dl}$  tends toward:

$$u_{z_0}^{dl} = \frac{\eta_{z_0}(R)}{\kappa_{z_0}(R) c} \quad (\text{C18})$$

which, if the scalelength of the dust and stellar emissivity distribution is the same, would have a flat distribution in  $R$ . In this optically thick limit one can also provide an analytical expression for the combination of direct and scattered light, since the scattered light will to a good approximation be re-absorbed and re-scattered close to the position of the originating stars. Under these circumstances the energy density of the radiation fields due to first order scattered light  $u^{sc,1}$  is:

$$u^{sc,1} = A u^{dl} \quad (\text{C19})$$

where  $A$  is the albedo. The total energy density of the radiation fields due to both direct and first order scattered light is:

$$u = u^{dl} + u^{sc,1} \quad (\text{C20})$$

By substituting Eq. C19 in Eq. C20 we obtain:

$$u = u^{dl} (1 + A) \quad (\text{C21})$$

Combining Eq. C18 with Eq. C21 we can obtain an accurate solution for the mid-plane radiation fields due to direct and first order scattered light for the very optically thick case:

$$u_{z_0} = \frac{\eta_{z_0}(R) (1 + A)}{\kappa_{z_0}(R) c} \quad (\text{C22})$$

Following from Eq. C19, the energy density due to the  $n$ th order scattered light  $u^{sc,n}$  is then given by:

$$u^{sc,n} = A u^{sc,n-1} = A^n u^{dl} \quad (\text{C23})$$

The total energy density of the radiation fields due to both direct and scattered light is:

$$u = u^{dl} + \sum_{n=1}^{\infty} u^{sc,n} \quad (\text{C24})$$

By substituting Eq. C23 in Eq. C24 we obtain:

$$u = u^{dl} \sum_{n=0}^{\infty} A^n = \frac{u^{dl}}{1 - A} \quad (\text{C25})$$

Combining Eq. C18 with Eq. C25 we can obtain an accurate solution for the total mid-plane radiation fields for the very optically thick case, in which the range of photons is small compared to  $z_d$

**Table C1.** The values of  $f_{esc}$  and  $f_{esc}^1$  for the case of one dust disk with  $\tau_B^f = 3.5$

$\lambda$	$f_{esc}^1$	$f_{esc}$
912	0.980	0.976
1350	0.976	0.956
1500	0.976	0.926
1650	0.976	0.926
2000	0.976	0.833
2200	0.980	0.833
2500	0.976	0.714
2800	0.966	0.658
3600	0.952	0.595

as well as being small compared to the scale over which opacity varies with  $R$ :

$$u_{z_0} = \frac{\eta_{z_0}(R)}{(1-A)\kappa_{z_0}(R)c} \quad (C26)$$

Finally we can write an approximate solution for the total mid-plane energy density for a disk with a scale-height equal to the scale-height of the stars, in which we relaxed the condition that the disk is optically thick in  $z$ , but in which we retained the condition that the disk is still optically thick in  $R$ . For this we combine Eq. C21 (for first order scattering) or Eq.C25 (for total scattering) with the exact solution for direct light from Eq. C16 to obtain:

$$u_{z_0}(R) = \frac{\eta_{z_0}(R)(1+A)}{\kappa_{z_0}(R)c} [1 - I''(R)] \quad (C27)$$

for direct plus first order scattering or

$$u_{z_0}(R) = \frac{\eta_{z_0}(R)}{(1-A)\kappa_{z_0}(R)c} [1 - I''(R)] \quad (C28)$$

for direct plus total scattered light.

Because in most real cases the solution is never completely optically thick, we include in the formula a further factor,  $f_{esc}$  ( $f_{esc}^1$  for first order scattering), which corrects for the extra escaping radiation which is not accounted by the approximation made for the scattering:

$$u_{z_0}(R) = f_{esc}^1 \frac{\eta_{z_0}(R)(1+A)}{\kappa_{z_0}(R)c} [1 - I''(R)] \quad (C29)$$

for direct plus first order scattering, or

$$u_{z_0}(R) = f_{esc} \frac{\eta_{z_0}(R)}{(1-A)\kappa_{z_0}(R)c} [1 - I''(R)] \quad (C30)$$

for direct plus total scattered light. The factors  $f_{esc}$  and  $f_{esc}^1$  depend on  $\tau_B^f$  and  $\lambda$ . In the very optically thick case  $f_{esc}$  and  $f_{esc}^1$  both take the value unity. In all other cases they can only be derived empirically, by calibrating them on radiative transfer calculations. In our formulation we consider  $f_{esc}$  (or  $f_{esc}^1$ ) a single number (independent of galactocentric position). This provides an estimate of the goodness of our approximation (for scattered light) for the centre of the disk, where the higher opacity is encountered, and therefore the best agreement is expected. Thus, the calibration is done by scaling the profiles at  $R = 0$ . The tables with the values of the  $f_{esc}$  and  $f_{esc}^1$  for  $\tau_B^f = 3.5$  are given in Table C1.

#### APPENDIX D: DERIVATION OF AN ANALYTICAL SOLUTION FOR RADIATION FIELDS IN THE MID-PLANE OF AN AZIMUTHALLY SYMMETRIC STELLAR DISK WITH TWO DUST DISKS

We take the stellar disk to have the same form as in Eq. C1. The two dust disks have also an exponential distribution in the vertical direction, but an arbitrary distribution in radial direction. This allows us to write the extinction coefficient  $\kappa(R, z)$  as a sum of the extinction coefficients of each dust disk:

$$\kappa(R, z) = \kappa_1(R, z) + \kappa_2(R, z) = \quad (D1)$$

$$= \kappa_{z_{d1}}(R) \exp\left(-\frac{z}{z_{d1}}\right) + \kappa_{z_{d2}}(R) \exp\left(-\frac{z}{z_{d2}}\right)$$

$$\kappa_{z_{d1}}(R) = \frac{\tau_1}{2z_{d1}} \quad (D2)$$

$$\kappa_{z_{d2}}(R) = \frac{\tau_2}{2z_{d2}} \quad (D3)$$

$$\tau = \tau_1 + \tau_2 \quad (D4)$$

where  $\kappa_1(R, z)$  and  $\kappa_2(R, z)$  are the extinction coefficients of the first and second dust disks, respectively,  $\kappa_{z_{d1}}(R)$  and  $\kappa_{z_{d2}}(R)$  are the mid-plane dust extinction coefficients of the first and second dust disks, respectively, and  $z_{d1}$  and  $z_{d2}$  are the scaleheights of the dust disks.

Following the same calculations as in Sect. C, we obtain the same equations as C3, C4, C5, but a different form from C6, namely:

$$\begin{aligned} \tau(l) &= \kappa_{z_{d1}}(R) \int_0^l \exp\left(\frac{-l \sin(\theta)}{z_{d1}}\right) dl \\ &+ \kappa_{z_{d2}}(R) \int_0^l \exp\left(\frac{-l \sin(\theta)}{z_{d2}}\right) dl \\ &= \frac{\kappa_{z_{d1}}(R) z_{d1}}{\sin(\theta)} \left[1 - \exp\left(-\frac{l \sin(\theta)}{z_{d1}}\right)\right] \\ &+ \frac{\kappa_{z_{d2}}(R) z_{d2}}{\sin(\theta)} \left[1 - \exp\left(-\frac{l \sin(\theta)}{z_{d2}}\right)\right] \end{aligned} \quad (D5)$$

We make the notations:

$$\alpha_1 = \frac{\kappa_{z_{d1}}(R) z_{d1}}{\sin(\theta)} = \frac{\tau_1}{2 \sin(\theta)} \quad (D6)$$

$$\alpha_2 = \frac{\kappa_{z_{d2}}(R) z_{d2}}{\sin(\theta)} = \frac{\tau_2}{2 \sin(\theta)} \quad (D7)$$

$$\beta_1 = \frac{\sin(\theta)}{z_{d1}} \quad (D8)$$

$$\beta_2 = \frac{\sin(\theta)}{z_{d2}} \quad (D9)$$

$$\gamma = \frac{\sin(\theta)}{z_s} \quad (D10)$$

$$\alpha = \alpha_1 + \alpha_2 \quad (D11)$$

With the new notation, the analogous of Eq. C10 becomes:

$$\begin{aligned} u_\theta d\theta &= d\theta \int_0^\infty u(l, \theta) dl \\ &= d\theta \frac{\eta_{z_0}(R) \cos(\theta) \exp(-\alpha)}{2c} I(\theta, \alpha_1, \alpha_2, \beta_1, \beta_2, \gamma) \end{aligned} \quad (D12)$$

where

$$I = \int_0^\infty \exp(-\gamma l) \exp(\alpha_1 e^{-\beta_1 l}) \exp(\alpha_2 e^{-\beta_2 l}) dl \quad (D13)$$

By further manipulating Eq. D13 we obtain:

$$I = \int_0^1 \xi^{\gamma-1} \exp(\alpha_1 \xi^{\beta_1} + \alpha_2 \xi^{\beta_2}) d\xi \quad (D14)$$

For

$$x = \frac{z_{d2}}{z_{d1}} \quad (\text{D15})$$

$$I = \left( \frac{x}{1+x} \right) \left( \frac{\omega_1}{2\kappa_{z01}} \right) I'' \quad (\text{D16})$$

where

$$I'' = \int_0^{\frac{\tau}{2\sin(\theta)}} \xi^{-\frac{1}{1+x}} \exp\left(\omega_1 \xi^{\frac{x}{1+x}} + \omega_2 \xi^{\frac{1}{1+x}}\right) d\xi \quad (\text{D17})$$

$$\omega_1(\theta) = \frac{\tau_1}{\tau^{\frac{x}{1+x}} (2\sin(\theta))^{\frac{1}{1+x}}} \quad (\text{D18})$$

$$\omega_2(\theta) = \frac{\tau_2}{\tau^{\frac{1}{1+x}} (2\sin(\theta))^{\frac{1}{1+x}}} \quad (\text{D19})$$

By substituting Eqs. D17 and D16 into Eq. D12 and integrating over  $\theta$  we obtain the analytic solution for the energy density in the mid-plane due to direct light from stars:

$$\begin{aligned} u_{z0}^{dl}(R) &= 2 \int_0^{\pi/2} u_\theta d\theta \quad (\text{D20}) \\ &= \left( \frac{x}{1+x} \right) \frac{\eta_{z0}}{\kappa_{z01} c} \int_0^{\pi/2} d\theta \cos(\theta) \exp\left(\frac{-\tau}{2\sin(\theta)}\right) \omega_1(\theta) I'' \end{aligned}$$

The formula in Eq. D20 can be reduced to Eq. C18 describing the case of a stellar disk with a single dust disk if one considers:  $\tau_2 = 0$ ,  $\omega_2 = 0$ ,  $\tau_1 = \tau$ ,  $\omega_1 = \omega$  and  $\kappa_{z01} = \kappa_{z0}$ .

Similarly to the case of one single dust disk, the solution including scattered light can be obtained by altering the solution for direct light with a term including the albedo  $A$ . Thus, the solution for the total mid-plane energy density is:

$$\begin{aligned} u_{z0}(R) &= f_{esc}^1 (1+A) \left( \frac{x}{1+x} \right) \frac{\eta_{z0}}{\kappa_{z01} c} \quad (\text{D21}) \\ &\times \int_0^{\pi/2} d\theta \cos(\theta) \exp\left(\frac{-\tau}{2\sin(\theta)}\right) \omega_1(\theta) I'' \end{aligned}$$

for the direct plus first order scattering or

$$\begin{aligned} u_{z0}(R) &= f_{esc} \left( \frac{1}{1-A} \right) \left( \frac{x}{1+x} \right) \frac{\eta_{z0}}{\kappa_{z01} c} \quad (\text{D22}) \\ &\times \int_0^{\pi/2} d\theta \cos(\theta) \exp\left(\frac{-\tau}{2\sin(\theta)}\right) \omega_1(\theta) I'' \end{aligned}$$

for the direct plus total scattered light.

In the case of a highly optically thick disk, this reduces to an exact expression:

$$u_{z0}(R) = \left( \frac{1}{1-A} \right) \left( \frac{x}{1+x} \right) \frac{\eta_{z0}}{\kappa_{z01} c} \quad (\text{D23})$$

**Table D1.** The values of  $f_{esc}$  for the case of two dust disks with  $\tau_B^f = 3.5$

$\lambda$	$f_{esc}$
912	0.970
1350	0.926
1500	0.909
1650	0.862
2000	0.826
2200	0.870
2500	0.699
2800	0.645
3600	0.581